THE ASTROPHYSICAL JOURNAL, 390:405–422, 1992 May 10

FORMATION OF A GIANT GALACTIC GASEOUS HALO: METAL ABSORPTION LINES AND HIGH-VELOCITY CLOUDS

FAN LI[1] AND SATORU IKEUCHI
Division of Theoretical Astrophysics, National Astronomical Observatory, Mitaka, Tokyo 181, Japan
Received 1991 August 5; accepted 1991 November 12

ABSTRACT

A Galactic gaseous halo formed through the interstellar disk-halo connection is simulated by means of a two-dimensional axisymmetric hydrodynamic code based upon the chimney model of the interstellar medium—a new version of a galactic fountain. Galactic rotation, heating processes by diffuse UV flux, and radiative cooling processes are taken into account. The resulting gaseous halo can be classified as belonging to one of three categories: wind-type halos, bound-type halos and cooled-type halos. The abundance of each ion of H, He, and heavy elements is calculated according to the hydrodynamic and thermal state of the halo gas. In this way, we try to reproduce the column densities of C IV, N V, O VI, and Si IV in the observed absorption lines of halo stars. Assuming that the radiatively cooled halo gas condenses into clouds due to thermal instabilities, we calculate the distribution and ballistic motions of the clouds in the Galactic gravitational field. These correspond to the high- and intermediate-velocity clouds observed at high Galactic latitudes. We find that a cooled-type halo with gas temperature between 5×10^5 and 10^6 K and density between 10^{-3} and 10^{-2} cm^{-3} at the disk-halo interface can reproduce the observational facts about our Galaxy.

Supposing that the metal absorption-line systems of QSOs arise from the halos of intervening galaxies formed by similar processes, we calculate features of the Ca II, Mg II, C IV, and Si IV absorption lines in various stages of the galaxies' evolution. We conclude that C IV systems greater than 50 kpc correspond to the wind-type halo. Contrarily, Mg II and Ca II systems can be detected in a very restricted region ($\lesssim$20 kpc).

Subject headings: cooling flows — galaxies: interstellar matter — Galaxy: halo — hydrodynamics — quasars: general

1. INTRODUCTION

The existence of a gaseous halo in our Galaxy was originally suggested theoretically by Spitzer (1956). After the discovery of a hot gas component, McKee & Ostriker (1977) proposed a supernova-dominated three-phase picture for the interstellar medium (ISM). Except for the prediction of a large filling factor of the hot gas in the ISM, this model also suggested a supernova-driven hot halo.

Our understanding of the ISM has changed dramatically because of the increasing amount of observational facts obtained in various bands in the last decade, such as H I supershells, worms (Heiles 1979, 1984), X-ray–emitting superbubbles (Cash et al. 1980), and an extended X-ray ridge on both sides of the Galactic center (Warwick et al. 1985; Koyama et al. 1986). These giant energetic structures can be understood only if supernova explosions are correlated in space and time (Heiles 1987, 1990). The structures formed by this process are metaphorically described as *chimneys* (Ikeuchi 1987, 1988; Norman & Ikeuchi 1989), since they are energetic enough to blow out of the Galactic disk and eject large amounts of energy and mass into the Galactic halo just like smoking chimneys.

There is also evidence for chimney structures in nearby spiral galaxies, such as H I holes in M31 and M33 (Brinks & Bajaja 1986; Deul & van der Hulst 1987; Deul & den Hartog 1990) and an H I hole surrounded by a symmetric expanding H I shell in M101 (Kamphuis et al. 1991a). Much more evidence for chimney structures is indicated in Bloemen (1990), although it is indirect. In brief, hot gas ejection from the galactic disk seems to be an important phenomenon of the ISM and deserves careful study.

Since thermal instabilities occur in the ejected hot gas due to the radiative cooling, cold clouds are expected to condense from the hot gas and fall ballistically to the Galactic plane under the influence of the Galactic gravitational field. These clouds take part in physical processes occurring in the Galactic disk, including star formation. In this way, the ISM as a whole forms a large-scale disk-halo circulation system. In Li & Ikeuchi (1989, 1990b, hereafter Papers I and III) we studied evolution of the ISM by investigating the interchanges among the hot, warm, and cold phases and disk-halo circulation based upon the chimney model. The observabilities of the chimney model was also studied (Li & Ikeuchi 1990a, hereafter Paper II) by considering certain spiral structures. We concluded that an ISM with many chimneys does offer a possible explanation of the observed supershells and X-ray ridge.

The gaseous halo around our Galaxy was confirmed observationally by absorptions in the spectra of early-type stars in the Galactic halo and beyond (Savage & de Boer 1979; Savage 1987). The column densities of Si IV, C IV, N V, and O VI are of the order of 10^{13}–10^{14} cm^{-2}, and the scale heights are of the order of 3–4 kpc (Savage & Massa 1987). Another feature of the gaseous halo is that the ratio of the column densities of C IV and Si IV is about 4.0 ± 1.6 and does not change with direction and height above the Sun (Savage & Massa 1987). If the gas is collisionally ionized, the temperature should be as high as about 10^5 K. The hot gas supplied from the disk might produce absorption as a form of these highly ionized ions.

Another observational fact about the Galactic halo is the existence of the so-called high-velocity clouds (HVCs) (Hulsbosch 1975; van Woerden et al. 1985). Recent whole-sky

[1] Postal address: Apartment 130, 1700 Hawthorne, El Paso, TX 79902.

surveys reveal that most of them are in fact not located at high Galactic latitudes but are concentrated toward the Galactic plane, and the amount of sky covered by positive-velocity clouds is about the same as that covered by negative-velocity gas (Bajaja et al. 1985; Hulsbosch & Wakker 1988; Wakker 1991; Wakker & van Woerden 1991). In the first two Galactic quadrants, negative-velocity clouds dominate, while in the last two quadrants positive-velocity clouds dominate. Moreover, high-velocity gas components are also observed in several external galaxies such as M101 (van der Hulst & Sancisi 1988) and NGC 6946 and NGC 628 (Kamphuis et al. 1991b; Kamphuis & Brinks 1991). The origin of HVCs is very important in understanding the ISM. Oort (1966, 1967, 1969, 1970) suggested the HVCs would be intergalactic gas infalling to the Galaxy. Obviously, this model has difficulty in explaining the clouds with positive velocities. Davis (1972, 1973) and Verschuur (1973) considered the possibility that HVCs are the outer warped spiral arms. They proposed that the observed velocities of the clouds are due to the effects of Galactic differential rotation. However, the clouds at high latitudes and anticenter still remain unexplained. Recent studies of Na I and Mg II absorption show that at least some HVCs contain metals (Songaila 1981; West et al. 1985; Songaila et al. 1985; Songaila, Cowie, & Weaver 1988; Danly 1989; de Boer 1989, 1990; van Woerden, Schwarz, & Wakker 1989; Robertson et al. 1991), which may imply that the HVCs are of galactic rather than intergalactic origin. To date, the best explanation of the HVCs is the so-called galactic fountain model.

The concept of a galactic fountain was first proposed by Shapiro & Field (1976) soon after the discovery of a hot gas component in the ISM. They argued that since the hot gas occupies a considerable fraction of the Galactic disk, the pressure gradient at disk-halo interface would push it upward into the Galactic halo. Radiative cooling causes this hot gas to undergo thermal instabilities (Field 1965), so that cold clouds condense out of the hot gas. Habe & Ikeuchi (1980) studied the structure of gaseous halos formed by this process. Bregman (1980) studied the distribution and motion of clouds formed by this process and showed that the main features of the high-velocity clouds can be reproduced if the temperature T_0 and density n_0 in the disk are in the ranges 7×10^5 K $< T_0 < 1.6 \times 10^6$ K and 5×10^{-4} cm^{-3} $< n_0 < 1.5 \times 10^{-3}$ cm^{-3}, respectively. Houck & Bregman (1990) examined a low-temperature galactic fountain to explain the H I gas in the lower halo region ($z < 1$ kpc). They found that a model with $T \sim 3 \times 10^5$ K gives the best explanation of this gas component. Bregman (1981) also examined whether the gaseous halo formed by a galactic fountain can explain the metal absorbing systems seen in QSO spectra. By integrating the clouds along a line of sight, he concluded that the model can reproduce the H I column density which is needed for the metal lines to be detectable. He did not, however, calculate ionization structures of halo gas according to the thermal state, which would be important to test whether the model can reproduce observed column densities of various ions observed as absorption systems.

The observed absorption lines in the spectra of QSOs can be divided into several categories. Within them, there are absorption lines due to the heavy elements with low and high ionization, such as Ca II and Na I in low-redshift systems ($Z < 0.3$), Mg II in intermediate-redshift systems ($0.3 < Z < 1$), and C IV and Si IV in high-redshift systems ($Z > 1$) (for a review see Blades 1987). The redshift ranges are due to observational constraints. They are thought to be halos of intervening galaxies. In some cases, the angles between the lines of sight to the QSO and to the galaxy are fairly large, which implies that the absorbing halos might be as large as $\sim$100 kpc (Bergeron 1987). Because they cover a large range of redshifts, QSO absorption-line systems are good probes for investigating the history of the universe from the epoch of galaxy formation to the present.

Since many new observational data have accumulated and new models have been proposed, it is necessary to recalculate the structure and evolution of the galactic halo according to the chimney model of the ISM, and find out what kinds of halo are expected under various disk activities. Supposing that the gaseous halo is formed by the gas supply from the disk through the chimneys, how does it evolve, and what does the structure look like? How does the halo change with different gas states in the disk?

In the present work we use a two-dimensional axisymmetric hydrodynamic code to calculate the structure of a Galactic halo formed by mass and energy ejection from the Galactic disk. We investigate whether the observed HVCs and absorption lines in our Galaxy can be reproduced by the present model, and what we can say about the different evolutionary stages of galaxies. The arrangement of this paper is as follows: In § 2 we describe the model and numerical method. In § 3 typical situations of gaseous halos are discussed. In § 4 model calculations of our Galaxy and nearby Sb galaxies are presented. Moreover, we discuss the formation of high-velocity clouds in the halo. In § 5 we simulate models for young galaxies and discuss the relation with absorption lines of QSOs. Finally, we summarize the results in § 6.

2. MODEL EQUATIONS AND NUMERICAL METHODS

2.1. *Model of the Galaxy*

In addition to pressure, the main force acting to halo gas is due to the Galactic gravitational potential Φ. It is composed of two components. One is due to the stellar component of the Galactic bulge and disk, which is axisymmetric. We use the model proposed by Miyamoto & Nagai (1975), which is written as

$$\Phi_{b,d}(r, z) = -\sum_{i=1}^{2} \frac{GM_i}{\{r^2 + [a_i + (z^2 + b_i^2)^{1/2}]^2\}^{1/2}}, \quad (1)$$

where $G = 6.6726 \times 10^{-8}$ dyn cm^2 g^{-1} is the gravitational constant and the subscript i corresponds to the bulge ($i = 1$) and disk ($i = 2$), with $a_1 = 0$, $b_1 = 0.495$ kpc, $M_1 = 2.05 \times 10^{10}\ M_\odot$ and $a_2 = 7.258$ kpc, $b_2 = 0.520$ kpc, $M_2 = 2.547 \times 10^{11}\ M_\odot$; r and z are the cylindrical coordinates parallel to the Galactic plane and perpendicular to it, respectively.

There is almost no doubt that galaxies have a dark halo component, because H I 21 cm observations show that the rotation velocity remains constant far beyond the luminous range. The spherically symmetric model for the dark halo of our Galaxy by Innanen (1973) is used in our calculation:

$$\Phi_h(r, z) = \frac{GM_h}{r_b}\left[\ln(1 + x) + \frac{1}{1 + x}\right] - \Phi_0, \quad (2)$$

where x is defined as

$$x = \frac{(r^2 + z^2)^{1/2}}{r_b},$$

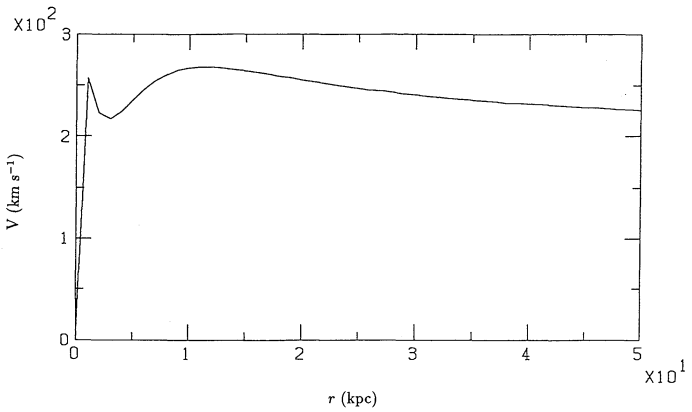

FIG. 1.—Rotation curve of the Galactic disk using the potential described by eqs. (1) and (2).

with $r_b = 13$ kpc, $M_h = 1.35 \times 10^{11}\ M_\odot$ and $\Phi_0 = 1.4 \times 10^{15}$ cm^2 s^{-2}.

This gives rise to a roughly flat rotation curve for the Galaxy with rotation velocity about 260 km s^{-1} near the Sun as shown in Figure 1.

Since our calculations are focused on late-type spiral galaxies, the gravitational potentials should all be similar to that described above. We use equations (1) and (2) in all the model calculations.

From the Galactic gravitational potential given above, we can calculate the critical temperature T_{cr} over which the hot gas in the disk will escape from the Galaxy and become a Galactic wind. If we neglect radiative cooling and assume that the gas escapes from the disk with sound speed, T_{cr} can be calculated as

$$T_{cr}(r) = \frac{2(\gamma - 1)}{\gamma(\gamma + 1)} \frac{\mu m_H}{k} \left[|\Phi(0, r)| - \frac{V_\phi^2}{2} \right], \quad (3)$$

where γ, μ, m_H, and k are the adiabatic index ($\gamma = 5/3$), the mean molecular weight ($\mu = 0.62$), the hydrogen mass, and the Boltzmann constant, respectively. V_ϕ is the rotation velocity of the gas in the disk with centrifugal force balanced with the gravitational force. Equation (3) is plotted in Figure 2. It is seen that T_{cr} smoothly decreases from about 6×10^6 K at $r = 1$ kpc as r increases. At the edge of the disk ($r = 15$ kpc), T_{cr} becomes 3×10^6 K. If the temperature of the gas is greater than this and radiative cooling is not important, the ejected gas will overcome the galactic potential to become a galactic wind. The density distribution of the gas in the disk is adopted in accordance with equation (1); it is described in § 2.5 and is shown in Figure 3.

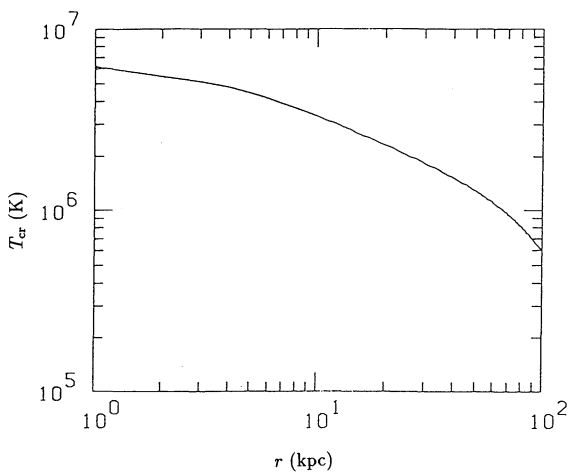

FIG. 2.—Critical temperature defined by eq. (3)

2.2. *Basic Equations and Numerical Method*

The motion of gas is described by the continuity and by the momentum and energy conservation equations of hydrodynamics as follows:

$$\frac{\partial \rho}{\partial t} + \nabla(\rho \boldsymbol{v}) = 0\,, \quad (4)$$

$$\frac{\partial(\rho \boldsymbol{v})}{\partial t} + \nabla(\rho \boldsymbol{v}\boldsymbol{v}) = -\nabla p - \rho \nabla \Phi\,, \quad (5)$$

$$\frac{\partial(\rho e)}{\partial t} + \nabla(\rho e \boldsymbol{v}) = -p \nabla \boldsymbol{v} - n^2 \Lambda + \Gamma\,, \quad (6)$$

where ρ, p, e, and $\boldsymbol{v}$ are mass density, pressure, specific thermal energy, and velocity, respectively. The ideal equation of state is used as $p = k\rho T/(\mu m_H)$ and $e = kT/[(\gamma - 1)\mu m_H]$. Λ is the functional fitting of the cooling rate calculated by Raymond, Cox, & Smith (1976) and Dalgarno & McCray (1972) as

$$\Lambda(T) = \begin{cases} 1.00 \times 10^{-24} T^{0.55} & (10^4\ \mathrm{K} < T \leq 10^5\ \mathrm{K})\,, \\ 6.20 \times 10^{-19} T^{-0.6} & (10^5\ \mathrm{K} < T \leq 4 \times 10^7\ \mathrm{K})\,, \\ 2.24 \times 10^{-27} T^{0.5} & (4 \times 10^7\ \mathrm{K} < T)\,. \end{cases} \quad (7)$$

Γ is the heating rate by UV flux, which is described in § 2.3.

The hydrodynamical equations are solved in two-dimensional axisymmetric coordinates. We use the Eulerian numerical scheme and an artificial viscosity described by Norman & Winkler (1986). The calculation is divided into two steps, i.e., the source step and the transport step. In the first, the fluid is accelerated by gas pressure, gravitational force, and artificial viscosity, and the internal energy is changed by the pressure and gravitational work, radiative cooling, and artificial viscosity. In the second, the resultant quantities are transported through the mesh by using the second-order monotonic interpolation (van Leer 1977). The computer code has been fully tested and used to calculate cosmological shock wave collisions by Yoshioka & Ikeuchi (1990), and we involve the angular momentum term to describe the galactic rotation.

2.3. *Heating by Diffuse UV Flux and Ionization Equilibrium*

Suppose there is a diffuse UV field with power-law spectrum

$$I(\nu) = I_0(\nu/\nu_0)^{-\alpha}\,, \quad (8)$$

where I_0 is the intensity at the Lyman limit frequency of hydrogen, ν_0. We use $I_0 = 10^{-23}$ ergs s^{-1} cm^{-2} s^{-1} Hz^{-1} and $\alpha = 1$ in the calculation of nearby galaxies. The gas is heated by the kinematic energy of ionized electrons of hydrogen and helium. The heating rate Γ is calculated as

$$\Gamma = \sum_i \Gamma_i = \int_{\nu_{0i}}^{\infty} 4\pi I_\nu \frac{\nu - \nu_{0i}}{\nu} \sigma_i(\nu) d\nu = 4\pi I_0 \epsilon_i G_i\,. \quad (9)$$

The summation is taken over H I, He I, and He II, and ν_{0i} and

$\sigma_i(\nu)$ are the ionization frequencies and absorption cross sections of the corresponding ions. The parameters listed in Table 2 of Black (1981) were used for ϵ_i and G_i.

In order to calculate the density of each ion of H, He, C, N, O, Mg, Si, and Ca in every mesh, we assume all the ions are in equilibrium between recombinations and collisional ionizations and photoionizations. This is reasonable if the ionization and recombination time scales are shorter than the dynamical time scale. Cosmic abundances are assumed for nearby galaxies. We use the results of photoionization cross sections by Reilman & Manson (1979), rates of radiative recombinations, dielectronic recombinations, and collisional ionizations by Shull & van Steenberg (1982), rates of low-temperature dielectronic recombinations by Nussbaumer & Storey (1983), and rates of recombinations and ionizations through charge transfer by Butler, Heil, & Dalgarno (1980). First, we calculate the density of electrons by solving ionization equilibrium equations of H and He iteratively. Then the resultant electron density is used to calculate rates of collisional ionizations and recombinations of heavier elements. The electrons which arise from the heavier elements are neglected, since they are far less abundant as long as the temperature is not too low.

2.4. *Cloud Formation and Motion in the Galactic Halo*

We suppose that the gas is condensed into clouds wherever the temperature in the mesh decreases below 10^4 K. Then the mesh is filled with gas with average gas density and dynamical properties of surrounding meshes, with conservation of total mass and momentum, but the pressure is unchanged, since usually thermal instabilities are isobaric processes (Field 1965). As is readily understood, this will cause an increase in the temperature of that mesh. The cloud is drawn out of the fluid and supposed to move ballistically with initial position and velocity just before it is formed in the Galactic gravitational field without any drag. The equations of motion of the clouds in the halo are described as

$$\frac{dV_z}{dt} = -\frac{\partial \Phi}{\partial z}, \tag{10}$$

$$\frac{dV}{dt} = -\frac{\partial \Phi}{\partial r} + \frac{J^2}{r^3}, \tag{11}$$

where J is the specific angular momentum of the cloud which is conserved during the motion.

Since our model is axisymmetric, the clouds are formed in rings. If we use the Galactic coordinates (l, b), the line-of-sight velocity relative to the local standard of rest of a cloud is as follows. We use $V_{z,r,\phi}$ to describe the velocity of the cloud in our calculated (r, z) coordinates, and $U_{z,r,\phi}$ to describe the line-of-sight velocity of the cloud relative to the local standard of rest. The velocity from the Galactic differential rotation is

$$U_\phi = (V_\phi r_\odot / r - V_{\phi\odot}) \sin l \cos b . \tag{12}$$

The velocity from the motion in the r-direction is

$$U_r = V_r \frac{(r^2 - r_\odot^2) \sin^2 b + z^2 \cos^2 b}{2rz \sin b} . \tag{13}$$

The velocity from the motion in the z-direction is

$$U_z = V_z \sin b . \tag{14}$$

Here the quantities with a subscript solar symbol are the values for the Sun, i.e., $V_{\phi\odot} = 260$ km s^{-1} and $r_\odot = 9$ kpc.

2.5. *Initial and Boundary Conditions*

The calculated region of the halo is $z \times r = 100$ kpc $\times$ 100 kpc. The region is divided into 200 $\times$ 100 uniform meshes.

As the initial condition, we suppose that the halo is filled with a uniform gas with temperature $T_i = 2 \times 10^4$ K and density $n_i = 10^{-10}$ cm^{-3}, which is thin enough to have less effect on the results. The gas rotates with velocity in centrifugal balance with the galactic gravity initially.

Boundary conditions at the disk-halo interface are assumed as follows. The disk-halo interface is at $z = 0.5$ kpc. The radius of the gas-ejecting disk is $r = 15$ kpc. We assume a density n_0 at $z = 0.5$ kpc, and $r = 0$. The gas is distributed throughout the disk in proportion to the stellar density as derived from equations (1). In Figure 3 the normalized density distribution in the disk is plotted. The temperature T_0 is assumed to be constant throughout the disk. The gas moves upward with sound speed $V_0 = (\gamma k T_0 / \mu m_H)^{1/2}$, which remains unchanged with time. Then the gas motion in the halo is calculated according to equations (4)–(6).

3. THREE TYPICAL CASES OF GASEOUS HALO

According to Habe & Ikeuchi (1980), there are three typical kinds of halo evolutionary patterns, depending on the properties of gas in the disk. If the gas temperature is higher than the critical temperature described in § 2.1, and radiative cooling is not important within the dynamical time, the gas becomes a galactic wind, which is called the wind-type halo. If the gas temperature is lower than the critical temperature, the gas is bound by the galactic gravitational field, which is called the bound-type halo. If the gas density is high enough so that the radiative cooling time is shorter than the dynamical time, the gas will be cooled quickly and cloud formation follows. These clouds will return to the galactic plane under the influence of galactic gravity. These features are verified in the present work, although the models are not completely the same. Cloud formation and motion in the halo are included as described in § 2.4. The calculated models are summarized in Table 1. Columns (1)–(5) of Table 1 show gas temperature, density, initial velocity, mass, and energy ejection rate at the disk-halo interface. Columns (6)–(10) show gas and cloud mass in the halo, cloud infalling rate, gas scale height at $r = 9$ kpc, and the resultant type of the gaseous halo.

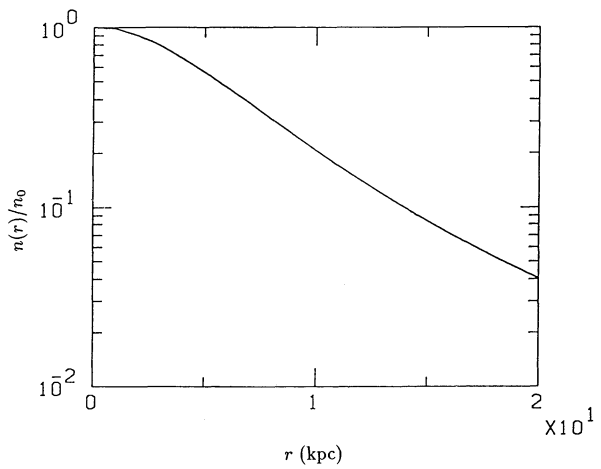

FIG. 3.—Density distribution in the Galactic disk normalized by the density at the center.

TABLE 1

SUMMARY OF ADOPTED PARAMETERS AND RESULTANT PROPERTIES OF CALCULATED GASEOUS HALOS

T_0 (K) (1)	n_0 (cm^{-3}) (2)	v_0 (km s^{-1}) (3)	$\dot{M}$ ($M_\odot$ yr^{-1}) (4)	$\dot{E}$ (ergs s^{-1}) (5)	M_g ($M_\odot$) (6)	M_c ($M_\odot$) (7)	$\dot{M}_{inf}$ ($M_\odot$ yr^{-1}) (8)	H (kpc) (9)	Type (10)
10^7	5×10^{-3}	280	15	2.7×10^{42}	2.6×10^9	...	...	45	Wind
8×10^6	5×10^{-3}	250	13	2.4×10^{42}	2.3×10^9	...	...	40	Wind
8×10^6	0.01	250	26	4.8×10^{42}	4.5×10^9	...	...	40	Wind
6×10^6	5×10^{-3}	220	12	2.0×10^{42}	2.0×10^9	...	...	35	Wind
6×10^6	0.01	220	24	4.0×10^{42}	4.0×10^9	...	...	35	Wind
6×10^6	0.03	220	70	7.8×10^{42}	1.3×10^{10}	3×10^9	...	35	Cooled
3×10^6	10^{-3}	150	1.6	1.1×10^{41}	6.3×10^8	...	...	25	Bound
3×10^6	5×10^{-3}	150	8.2	5.4×10^{41}	10^9	...	...	20	Bound
10^6	10^{-3}	90	1	3.3×10^{40}	2×10^8	...	...	10	Bound
10^6	5×10^{-3}	90	4.7	1.6×10^{41}	5×10^8	9×10^7	2	4	Cooled
10^6	0.01	90	9.5	3.3×10^{41}	6×10^8	2.5×10^8	5	3	Cooled
8×10^5	10^{-3}	80	0.9	2.5×10^{40}	1.5×10^8	...	...	6	Bound
8×10^5	5×10^{-3}	80	4.3	1.3×10^{40}	4.3×10^8	8.8×10^7	2	3	Cooled
8×10^5	0.01	80	8.9	2.5×10^{40}	7.5×10^8	1.6×10^8	4.5	3	Cooled
5×10^5	10^{-3}	64	0.7	1.8×10^{40}	1.6×10^8	...	...	4	Bound
5×10^5	5×10^{-3}	64	3.4	9×10^{40}	2.5×10^8	3.5×10^7	1	3	Cooled
5×10^5	0.01	64	6.7	1.8×10^{41}	6.1×10^8	9×10^7	3.3	2	Cooled
2×10^5	10^{-3}	40	0.5	1.2×10^{40}	1.1×10^8	9×10^6	0.3	2	Cooled
2×10^5	5×10^{-3}	40	2.4	6×10^{40}	5.1×10^8	3.6×10^7	1.2	1	Cooled

3.1. *Wind-Type Halo*

As an example of the wind-type halo, we calculate the halo evolution when the temperature and density at the disk-halo interface are $T_0 = 10^7$ K and $n_0 = 5 \times 10^{-3}$ cm^{-3}, respectively. As seen in Figure 2, this temperature is higher than the critical one even for the innermost region of the galaxy, and all the ejected gas from the disk will leave the galaxy to become a galactic wind. Since the gas density is low, radiative cooling is not efficient. We show the structure of temperature and density with velocity vectors in Figure 4.

The gas is once accelerated upward and outward due to the pressure gradient. The velocities near the z-axis are always smaller than elsewhere, since the gravitational forces are stronger. The centrifugal force which arises from the rotation of the gas in the galactic plane balances with the gravitational force. As the gas moves upward, the gravitational force

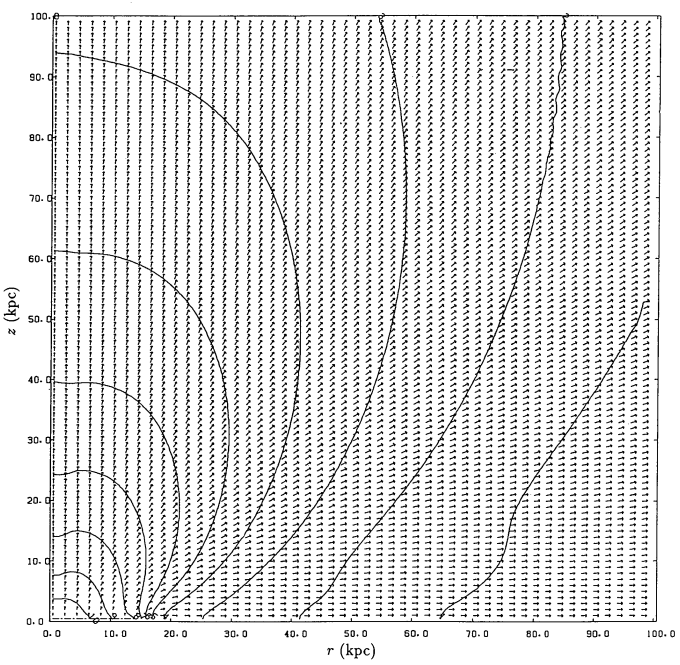

FIG. 4a

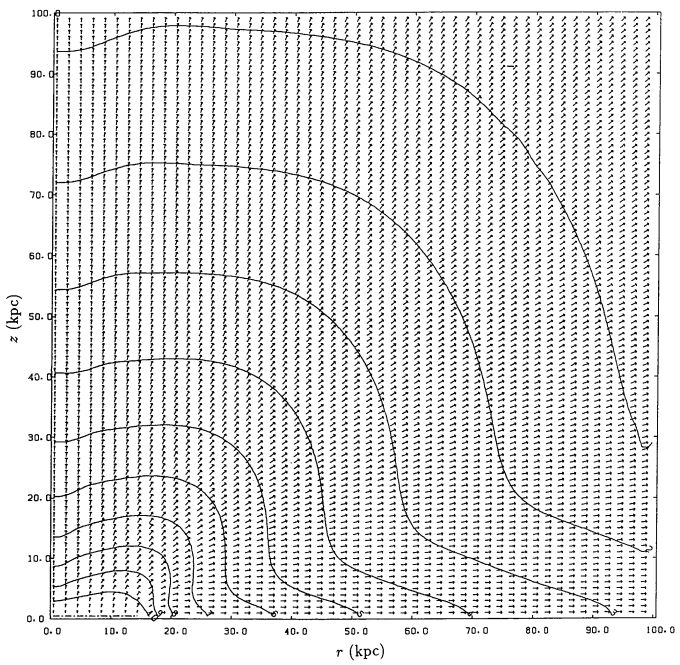

FIG. 4b

FIG. 4.—(*a*) Contours of isodensity (cm^{-3}) and velocity field (km s^{-1}) at $t = 3.3 \times 10^8$ yr for the model $T_0 = 10^7$ K and $n_0 = 5 \times 10^{-3}$ cm^{-3}. The log density levels are, from 1 to 10, −5.590, −5.275, −4.961, −4.648, −4.332, −4.017, −3.703, −3.388, −3.073, and −2.759, respectively. The maximum velocity is 710 km s^{-1}. (*b*) Same as (*a*), but with contours of isotemperature (K). The log temperature levels are, from 1 to 10, 5.529, 5.674, 5.819, 5.965, 6.111, 6.257, 6.402, 6.548, 6.694, and 6.840, respectively.

becomes weaker, and the centrifugal force becomes dominant, so that the gas moves outward in the r-direction causes the gas to expand in both the z- and r-directions. But the motion in the z-direction is about one-third faster. We find a steady state of the halo when $t \sim 3.3 \times 10^8$ yr, which is the dynamic time necessary for the gas to reach the distance 100 kpc as shown in Figures 4*a* and 4*b*. As is seen, the halo structure is very regular. The velocity increases upward and outward, while the temperature and density decrease. No discontinuity exists in the whole halo region. The gas moves with supersonic speed. The region with density greater than 10^{-4} cm^{-3} and temperature higher than 10^6 K extends to $z \sim 40$ kpc for $r < 15$ kpc. The mass and energy ejection rate at the disk-halo interface are 15 $M_\odot$ yr^{-1} and 2.7×10^{42} ergs s^{-1}, respectively. The rate of gas flowing out of the halo is nearly balanced by the gas supply from the galactic disk. The total mass in the calculated halo region is about 3×10^9 $M_\odot$. This is a steady state galactic wind.

The structure of a wind-type halo does not change significantly even if the parameters at the disk-halo interface change, as long as the gas temperature is higher than T_{cr} and radiative cooling is not effective.

Since the gas temperature is high while density is low, the gas is nearly fully ionized.

3.2. *Bound-Type Halo*

As an example of a bound-type halo, we calculate the halo evolution when the temperature and density at the disk-halo interface is $T_0 = 10^6$ K and $n_0 = 10^{-3}$ cm^{-3}, respectively. As seen in Figure 2, this temperature is lower than the critical one, and the ejected gas from the disk is bound by the galactic gravitational field. Radiative cooling is not effective because the gas density is low, and the cooling time is considerably longer than the dynamic time. We show the isodensity and isotemperature contours with velocity vectors in Figure 5 at the evolution time $t = 2.5 \times 10^8$ yr.

Compared with the wind-type halo described above, the gas is limited in the lower halo region but is expelled considerably outward. This is because the gravitational force in the z-direction overwhelms the pressure gradient, while the centrifugal force overwhelms gravitational force in the r-direction. The region with density greater than 10^{-5} cm^{-3} is limited within $z \sim 10$ kpc but extended to $r \sim 40$ kpc. In the region $r < 20$ kpc, the gas in the halo falls down and collapses with the wind flowing out from the disk. This gives rise to a somewhat complex temperature structure compared with the wind-type halo. Instead of adiabatic cooling, there is a banding structure in which the temperature increases due to the gas compression. All the gas will eventually return to the outer galactic plane, since they are not energetic enough to run away from the galaxy. The mass and energy ejection rate at the disk-halo interface are 1.0 $M_\odot$ yr^{-1} and 3.3×10^{40} ergs s^{-1}, respectively. The total mass in the calculated halo region is about 2×10^8 $M_\odot$.

The column densities of C IV, N V, and Si IV integrated vertically from the Sun are still much lower than those observed in the Galactic halo.

If the temperature of the ejected gas increases, the scale height of the gaseous halo of bound type can also increase more, as seen in Table 1, and the structure of the halo can be very similar to wind-type ones except for the region near z-axis.

3.3. *Cooled-Type Halo*

When the gas density is high enough, radiative cooling will become efficient before long, and the gas will condense into cold clouds due to thermal instability. This is called a cooled-type halo. The cooled-type halos can be divided into two classes according to their dynamical behavior. If the temperature of the disk gas is high, the dynamical behavior is similar to that of the wind-type halo globally, but cloud condensation occurs in a local dense region. We call the resulting halo a *w-c* type. It will be shown later that in the *w-c* type halo

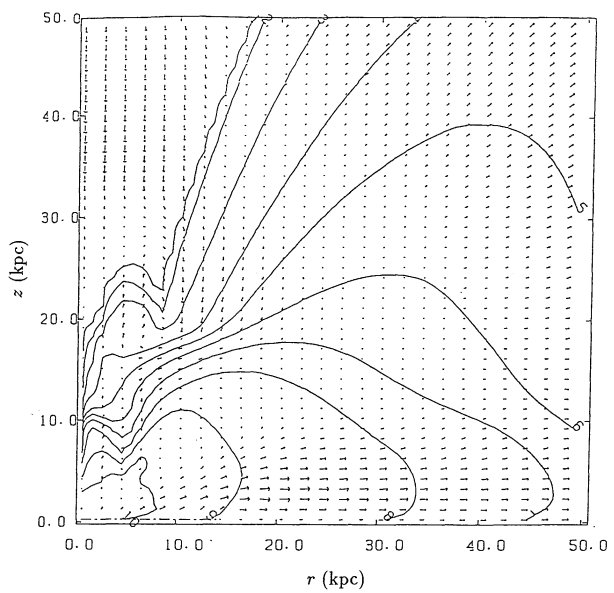

FIG. 5*a*

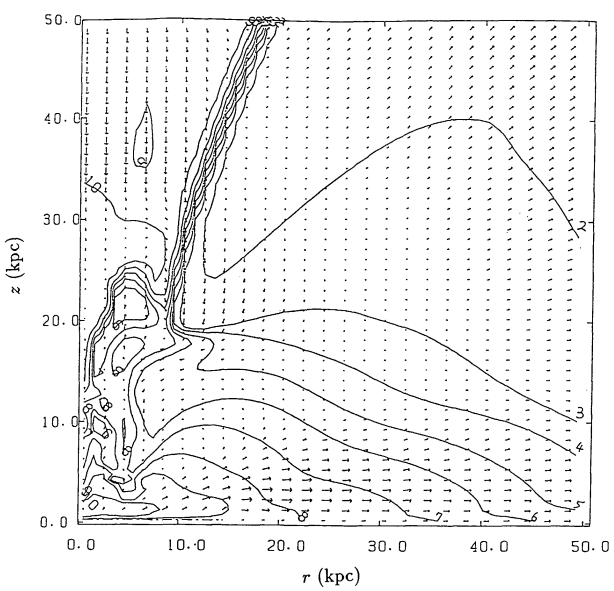

FIG. 5*b*

FIG. 5.—(*a*) Same as Fig. 4*a*, but for the model $T_0 = 10^6$ K and $n_0 = 10^{-3}$ cm^{-3} at $t = 2.5 \times 10^8$ yr. The log density levels are, from 1 to 10, −9.738, −9.023, −8.307, −7.592, −6.877, −6.161, −5.446, −4.731, −4.015, and −3.300, respectively. The maximum velocity is 240 km s^{-1}. (*b*) Same as (*a*), but with contours of isotemperature (K). The log temperature levels are, from 1 to 10, 4.260, 4.491, 4.723, 4.954, 5.186, 5.417, 5.649, 5.881, 6.112, and 6.344, respectively.

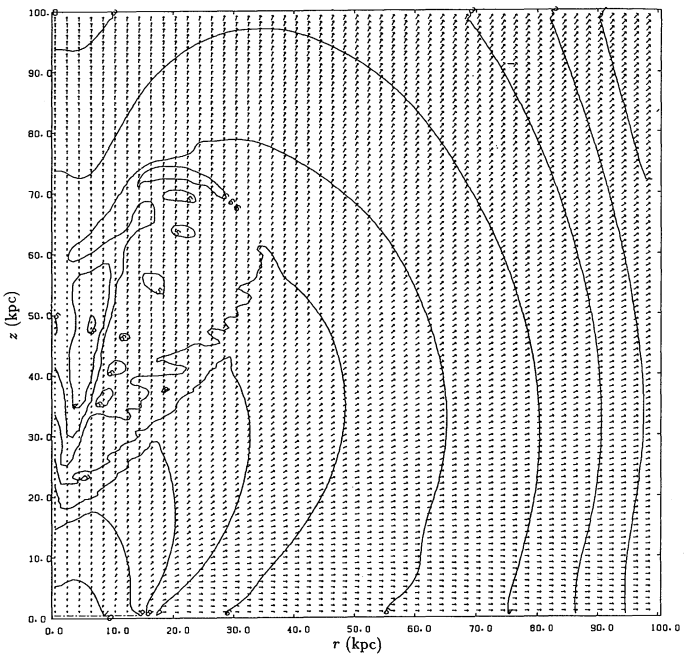

FIG. 6a

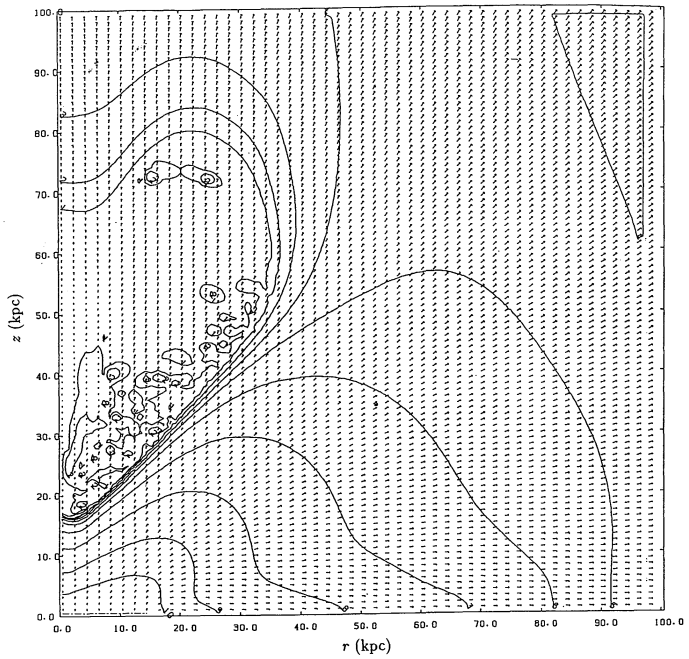

FIG. 6b

FIG. 6.—(*a*) Same as Fig. 4*a*, but for the model $T_0 = 6 \times 10^6$ K and $n_0 = 3 \times 10^{-2}$ cm^{-3} at $t = 4.7 \times 10^8$ yr. The log density levels are, from 1 to 10, −6.593, −6.100, −5.607, −5.114, −4.620, −4.127, −3.634, −3.140, −2.647, and −2.154, respectively. The maximum velocity is 520 km s^{-1}. (*b*) Same as (*a*), but with contours of isotemperature (K). The log temperature levels are, from 1 to 10, 4.055, 4.326, 4.597, 4.868, 5.139, 5.410, 5.681, 5.952, 6.223, and 6.493, respectively.

clouds are formed high above the galactic disk, and initial velocities of the clouds are always very high, so that it takes a long time for them to return to the galactic disk. On the other hand, when the temperature of the ejected disk gas is lower than T_{cr} and the density is high, a large amount of gas will condense into clouds before it moves far, and formed clouds ballistically fall back to the disk. The halo thus formed is called a *b-c* type. We will show that the gaseous halo, like our own, belongs to this *b-c* type.

3.3.1. *w-c Type Halo*

As an example of a *w-c* type halo, we calculate the halo evolution when the temperature and density at the disk-halo interface are $T_0 = 6 \times 10^6$ K and $n_0 = 3 \times 10^{-2}$, respectively. We show the isodensity and isotemperature contours with velocity vectors in Figure 6 at the evolution time $t = 4.7 \times 10^8$ yr. We can see that the velocity field is very similar to the wind-type halo. However, there arises a cloud formation

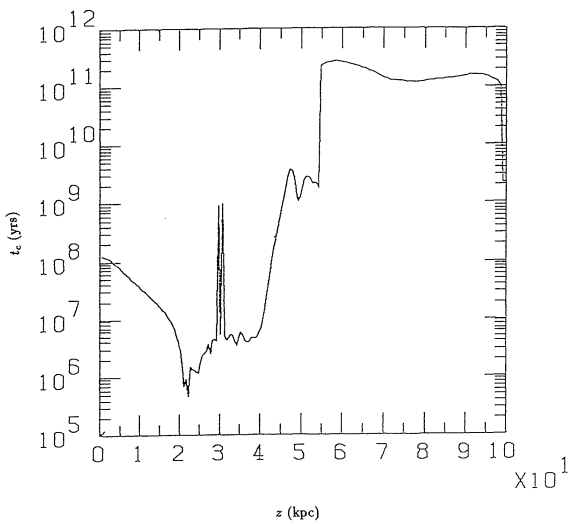

FIG. 7a

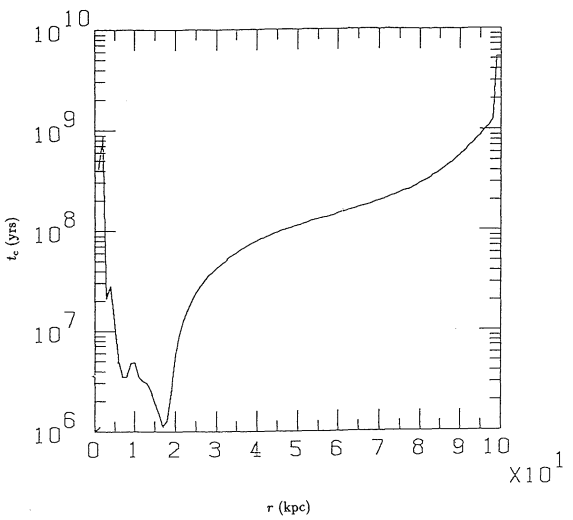

FIG. 7b

FIG. 7.—(*a*) Variation of cooling time along $r = 10$ kpc for the model $T_0 = 6 \times 10^6$ K and $n_0 = 3 \times 10^{-2}$ cm^{-3} at $t = 4.7 \times 10^8$ yr. Rapid variations are due to the removal of clouds. (*b*) Same as (*a*), but along $z = 30$ kpc.

region where we see clumps and discontinuities of density and temperature. This region is located at 0 kpc $< r <$ 30 kpc and 20 kpc $< z <$ 60 kpc. As radiative cooling becomes efficient, the temperature decreases rapidly, and cloud formation takes place due to thermal instability. In Figure 7 the variation of cooling time is shown. The cooling time along the vertical line at $r = 10$ kpc first decreases. At $z \sim 20$ kpc, it reaches a minimum value of $t_c \sim 10^6$ yr. Then the cooling time increases and becomes $\sim 10^9$ yr at $z \sim 45$ kpc, as seen in Figure 7*a*. Rapid changes occur due to the removal of clouds. Similarly, cooling time variation along $z = 30$ kpc is shown in Figure 7*b*, where we can clearly see that the region of cloud formation is in the range 0 kpc $< r <$ 20 kpc. The mass and energy ejection rate at the disk-halo interface are 72 $M_\odot$ yr^{-1} and 1.3×10^{43} ergs s^{-1}, respectively. The total mass of the clouds in the halo is about 3×10^9 $M_\odot$ while the amount of hot gas is about 5 times more. The initial velocities of the clouds when they are formed range from $\sim$200 to 400 km s^{-1}, as can be seen in Figure 6. Most of the clouds will return to the disk in a time scale of several times 10^9 yr or longer. Some of the clouds are energetic enough to escape from the galaxy eventually. Because the amount of clouds is very large, they will trigger bursts of star formation after they return to the galactic disk, and the disk-halo system will undergo periodic evolution (Papers I and III). This will be examined in future in relation to the time-variable disk activities.

3.3.2. *b-c Type Halo*

As an example of a *b-c* type halo, we calculate the halo evolution when the temperature and density at the disk-halo interface are $T_0 = 10^6$ K and $n_0 = 5 \times 10^{-3}$ cm^{-3}, respectively. We show the isodensity and isotemperature contours with velocity vectors in Figure 8 at the evolution time $t = 3.4 \times 10^8$ yr. We can see that the density and velocity structure are not so different from those of the bound-type halo described above. However, in the region $r \sim 0$–20 kpc and $z \sim 0$–10 kpc the temperature structure is quite different. This is just the region where cloud condensation takes place which can be called the cloud formation layer. The description of the resultant distribution of clouds and column densities of ions is presented in the next section. The mass and energy ejection rate at the disk-halo interface are 4.7 $M_\odot$ yr^{-1} and 1.6×10^{41} ergs s^{-1}, respectively. The total mass of the clouds in the halo is about 9×10^7 $M_\odot$, while the amount of gas is about 10^8 $M_\odot$. The resultant cloud infalling rate to the disk is about 3 $M_\odot$ yr^{-1}. Further details of this case are described in § 4.1 in relation to the Galactic halo.

In Figure 9 we classify the calculated models and resultant properties of the halo.

4. MODEL OF OUR GALAXY AND NEARBY LATE-TYPE SPIRALS

As described, the existence of a gaseous halo in our Galaxy has been confirmed by the observations of absorptions due to ionized heavy elements in the spectra of stars in the Galactic halo and beyond. Also, many high-velocity H I clouds in high latitudes have been discovered by 21 cm emission lines. They distribute all around the sky. One of the purposes of the present work is to find out whether interstellar disk-halo interactions based upon the chimney model can explain these observational facts. We find out that *b-c* type halos with 5×10^5 K $\leq T_0 \leq 10^6$ K and 10^{-3} cm^{-3} $< n_0 < 10^{-2}$ cm^{-3} are consistent with the observed results of our Galaxy.

4.1. *Our Galaxy*

In Figure 10 we show the column densities of C IV, N V, O VI, and Si IV integrated vertically from the position of the Sun ($r = 9$ kpc) and the corresponding N(Si IV)/N(C IV) ratio according to the result of the parameters $T_0 = 10^6$ K and $n_0 = 5 \times 10^{-3}$ cm^{-3}. The observational data in Figure 5 of Savage & Massa (1987) are also plotted. The resultant column den-

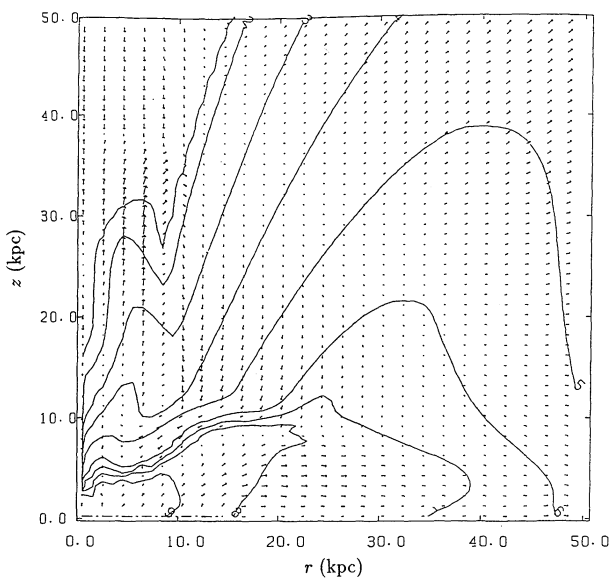

FIG. 8*a*

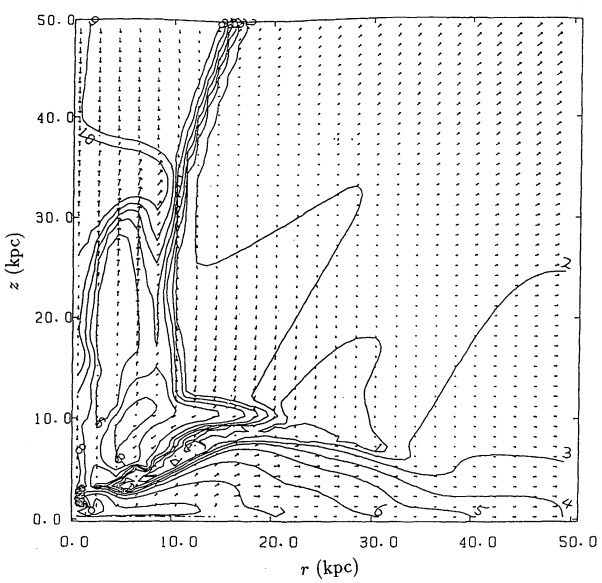

FIG. 8*b*

FIG. 8.—(*a*) Same as Fig. 4*a*, but for the model $T_0 = 10^6$ K and $n_0 = 5 \times 10^{-3}$ cm^{-3} at $t = 3.4 \times 10^8$ yr. The log density levels are, from 1 to 10, −9.629, −8.759, −7.961, −7.127, −6.293, −5.459, −4.625, −3.792, −2.958, and −2.124, respectively. The maximum velocity is 290 km s^{-1}. (*b*) Same as (*a*), but with contours of isotemperature (K). The temperature levels are, from 1 to 10, 4.176, 4.439, 4.701, 4.964, 5.226, 5.489, 5.751, 6.014, 6.276, and 6.539, respectively.

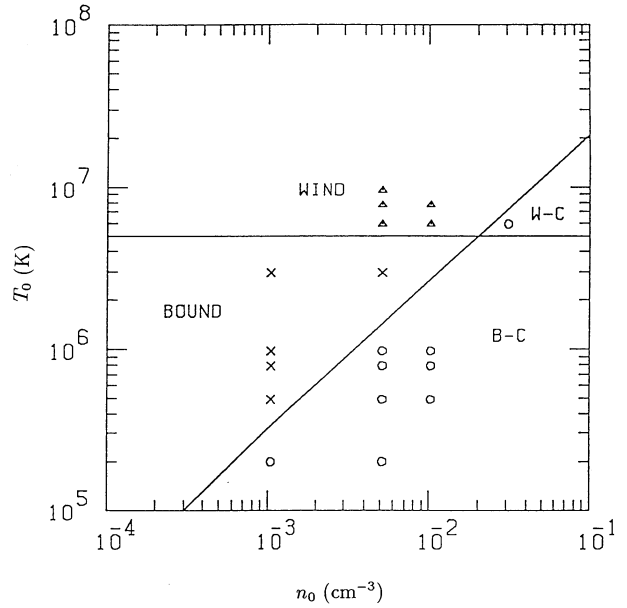

FIG. 9.—Summary of calculated models and classification of evolution in an $n_0 - T_0$ diagram. *Triangle*: wind type; *cross*: bound type; *circle*: cooled type. They are also summarized in Table 1.

sities are consistent with observations of absorption lines in the spectra of halo stars (Savage 1987) above $z \sim 2$ kpc, at last within a factor of 2. The results do not change much in the range 0 kpc $< r \leq 30$ kpc. We predict from our calculation that the column density of O VI should be higher than 10^{14} cm^{-2} if we observe the spectra of halo stars above the scale height of the halo. Moreover, we find that less highly ionized ions are more abundant than highly ionized ions in *b-c* type halos. For example, the column density of C II is about 10 times greater than that of C IV. We will mention in the next section that in our model describing C IV absorption-line systems of quasars with high gas temperature, the amount of C IV becomes greater than that of C II. This is also consistent with observations (Wolfe 1983; Danly, Blades, & Norman 1987). Our results indicate that the Galactic absorption corona and QSO absorption-line systems have a similar origin, but with different parameters in the disk-halo interface.

In our model, the gas is ejected from $z = 500$ pc with temperature $T_0 = 10^6$ K, which is higher than the model of Itoh & Ikeuchi (1988), who assume an isothermal and exponential distribution of gas. The gas temperature falls to $\sim 10^5$ K at about $z \sim 2$ kpc, where the recombinations take place. So the variation of column densities and the N(C IV)/N(Si IV) ratio is different from their result at $z < 2$ kpc. However, if we shift the vertical axis to 2 kpc, the variation becomes similar to their result. The model of Itoh & Ikeuchi (1988) is consistent with the *IUE* observations (Savage & Massa 1987) at lower height, which may indicate that an isothermal gas component in addition to the ejected hot gas component with lower temperature ($\sim 10^5$ K) below the height $z \sim 2$ kpc is needed.

In Figure 11 we show a relation between position and line-of-sight velocity distribution of the clouds in Galactic coordinates. Imagine that we are observing the clouds at the solar position, and divide the whole sky into several regions in (l, b) coordinates. Each cloud ring is broken up into 100 "clouds" and they are randomly distributed along the circle. The area of the circle in each region is proportional to the percentage of the "clouds" in that region, and the circle is divided into several sectors filled with different patterns which correspond to different velocity ranges (i.e., *black*: $U \leq -220$ km s^{-1}; *diagonal grid*: -220 km s$^{-1} < U \leq -130$ km s^{-1}; *hatched*: -130 km s$^{-1} < U \leq -80$ km s^{-1}; *white*: -80 km s$^{-1} < U < 80$ km s^{-1}; *crosses*: 80 km s$^{-1} \leq U < 130$ km s^{-1}; *wavy lines*: 130 km s$^{-1} \leq U < 220$ km s^{-1}; *cubes*: $U \geq 220$ km s^{-1}). The angle of each sector corresponds to the percentage of the clouds in that velocity range. In Figure 11a we show the percentages of clouds with positive and negative line-of-sight velocities. We see that about 90% of the clouds are located in the lower latitude region ($b \leq 40°$), although some clouds can be seen at high latitudes. The most populated region is within 60° on both sides of the Galactic center, and $b < 20°$ where nearly 59% of the clouds are seen. In the first and second quadrants, most of the clouds have negative velocities, while in the third and fourth quadrants, positive-velocity clouds dominate. This is consistent with the results of the whole-sky survey of HVCs in our Galaxy (Bajaja et al. 1985). It is readily understood from equations (12) and (14) that when V_ϕ is much greater than V_z, the sign of the line-of-sight velocity is determined by the difference between the angular velocities of the Sun and the cloud. As the angular momentum is conserved during the motion, the angular velocity of the cloud is less than that of the Sun as long as the r-coordinate of the cloud is greater than the radius of the solar circle. Since most of the clouds are located out of the solar circle in our model, it is natural for us to observe the velocity distribution described above. Most of the clouds are located lower than $z = 10$ kpc but can move fairly far in the r-direction. The small effect of V_z causes asymmetric distribution between the first two and last two quadrants. Next, we further divide the velocities of the clouds into several ranges for both positive and negative velocities as shown in Figure 11*b*. The effects of differential rotation are most obviously seen in the regions $60° < l < 120°$ and $240° < l < 300°$, with lower latitudes as is readily understood from equation (12). In other regions (e.g., $300° < l < 360°$ and $40° < b < 60°$), we can see the effects of z-motion of the clouds. Clouds with large velocities, both positive and negative, are seen at low-latitude regions, and at high latitudes most clouds have smaller line-of-sight velocities. On the other hand, the intermediate-velocity clouds with $|U| < 80$ km s^{-1} can be seen at almost any regions. These are all roughly consistent with observations.

Our model cannot explain the observed asymmetry of the HVCs between $b > 0$ and $b < 0$. This asymmetry might be caused by interactions of our Galaxy with neighboring galaxies like the Large and Small Magellanic Clouds.

The results described above do not change much with the parameters in the range mentioned in the beginning of this section, except for lower temperatures, which result in a lower scale height of gas and cloud distributions, lower column density, and a smaller amount of clouds. When the temperature becomes lower than 2×10^5 K, the scale-height of the cloud distribution is too low to be consistent with the observations.

4.2. *Nearby Galaxies*

We believe that nearby, normal late-type spirals like M31 and M33 can also be described by similar models. In Figure 12*a* we show the variation of the column densities with the r-coordinate which are integrated along r = constant for the model described above. This corresponds to the observation of

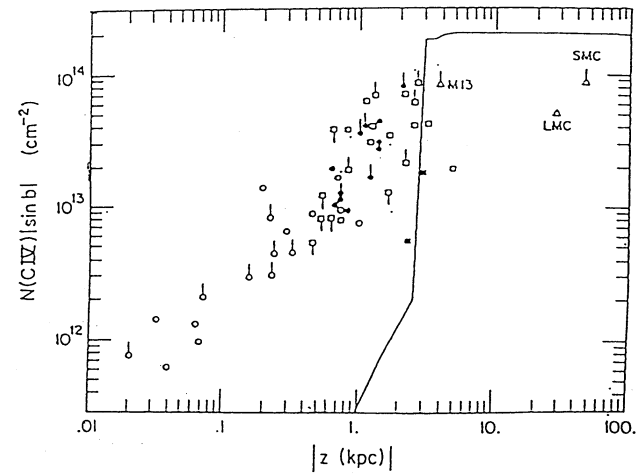

FIG. 10*a*

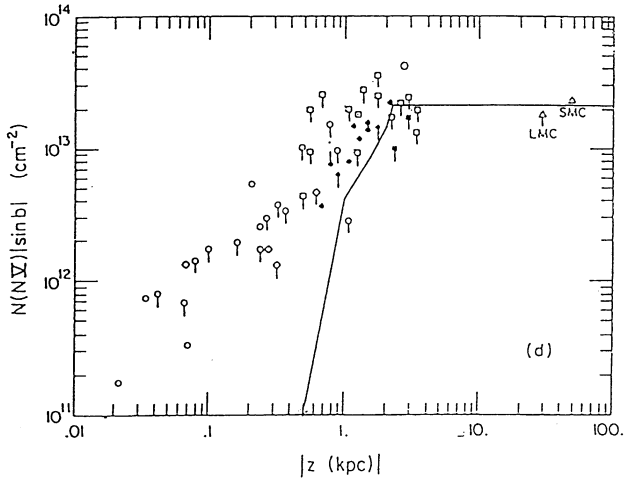

FIG. 10*b*

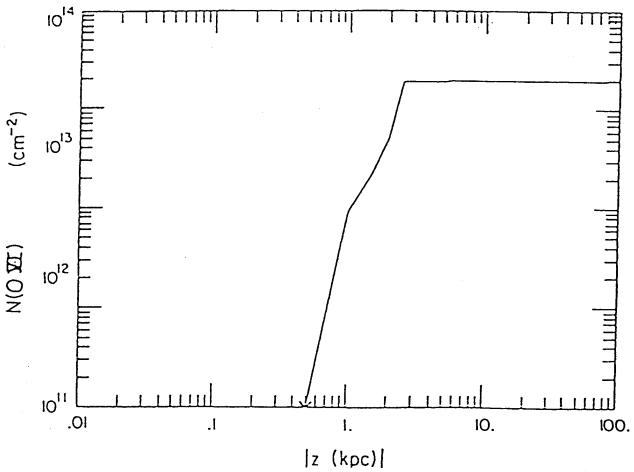

FIG. 10*c*

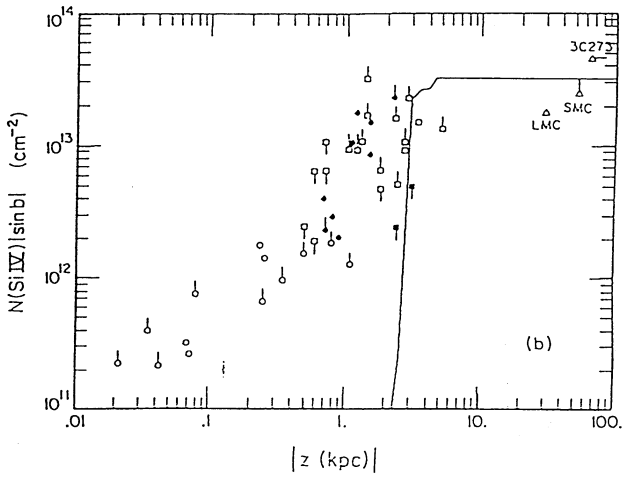

FIG. 10*d*

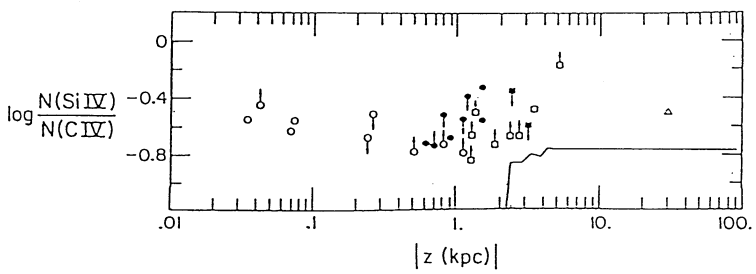

FIG. 10*e*

FIG. 10.—Column densities integrated vertically from the position of the Sun ($r = 9$ kpc) of (*a*) C IV, (*b*) N V, (*c*) O VI, (*d*) Si IV, and (*e*) the ratio of Si IV and C IV for the model $T_0 = 10^6$ K and $n_0 = 5 \times 10^{-3}$ cm^{-3}. The observational data in Fig. 5 of Savage & Massa (1987) are also plotted.

a nearby face-on galaxy like our own. It is seen that the column densities do not change much until $r \sim 30$ kpc. This means that we can observe the absorptions within $r \leq 30$ kpc from the center of the galaxy. In Figure 12*b*, we show the variation of the column densities with the z-coordinate which are integrated along z = constant for the model described above. This corresponds to the observation of a nearby edge-on galaxy similar to our own. It is seen that the high column density region is restricted within $z \sim 10$ kpc, which is fairly low, since the temperature is low. Rapid variations are due to the discontinuity of the thermal structure of the galaxy.

5. MODEL OF QSO ABSORPTION-LINE SYSTEMS

Absorption-line systems observed in spectra of quasars are believed to arise from giant gaseous halos around galaxies lying between the quasars and us. The size of these halos, especially the C IV systems, is estimated to be several tens of

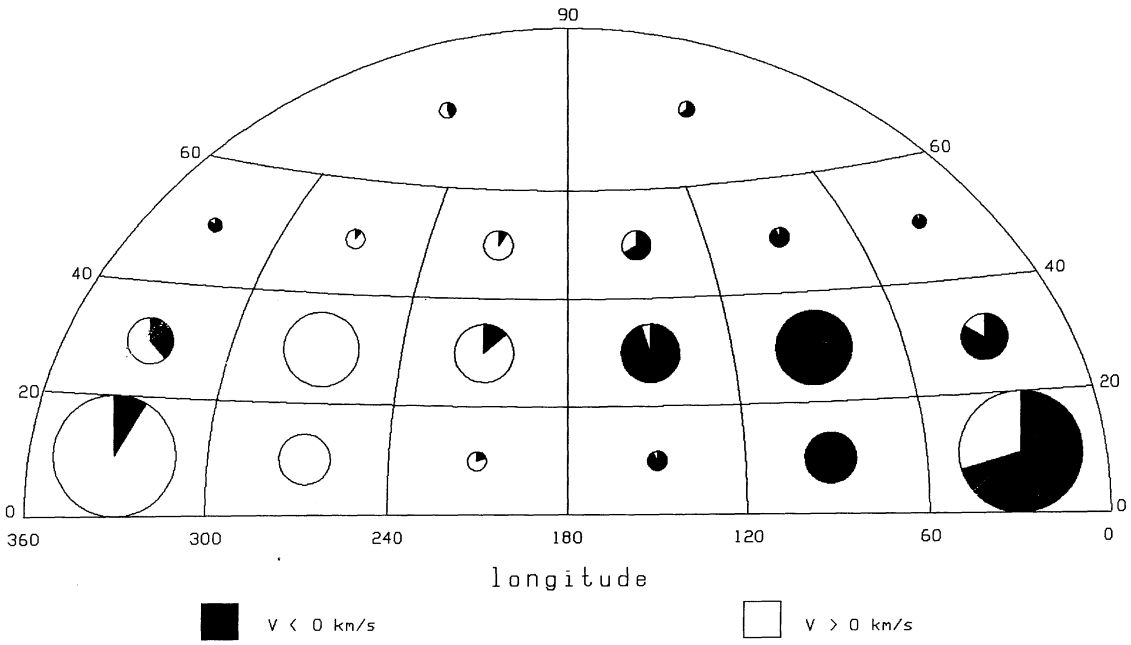

FIG. 11*a*

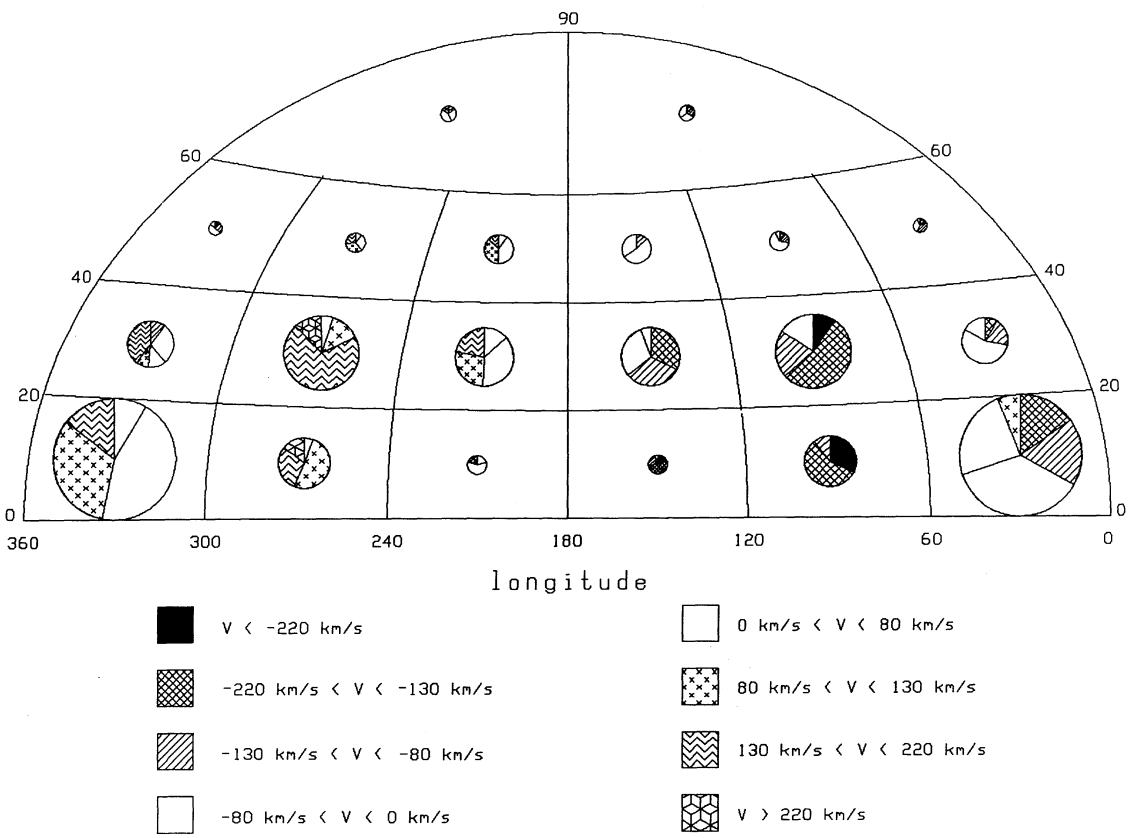

FIG. 11*b*

FIG. 11.—(*a*) Position and line-of-sight velocity distribution of clouds in Galactic coordinates for the model of our Galaxy ($T_0 = 10^6$ K and $n_0 = 5 \times 10^{-3}$ cm^{-3}). The area of the circle in each region is proportional to the percentage of the clouds in that region. The angle of the black sector corresponds to the percentage of negative-velocity clouds and the angle of the white sector corresponds to the percentage of positive-velocity clouds. (*b*) Same as (*a*), but the velocity distribution is given in detail: $U \leq -220$ km s^{-1} (*black*), -220 km s^{-1} $< U \leq -130$ km s^{-1} (*diagonal grid*), -130 km s^{-1} $< U \leq -80$ km s^{-1} (*hatched*), -80 km s^{-1} $< U < 80$ km s^{-1} (*white*: intermediate-velocity clouds), 80 km s^{-1} $\leq U < 130$ km s^{-1} (*crosses*), 130 km s^{-1} $\leq U < 220$ km s^{-1} (*wavy lines*), $U \geq 220$ km s^{-1} (*cubes*).

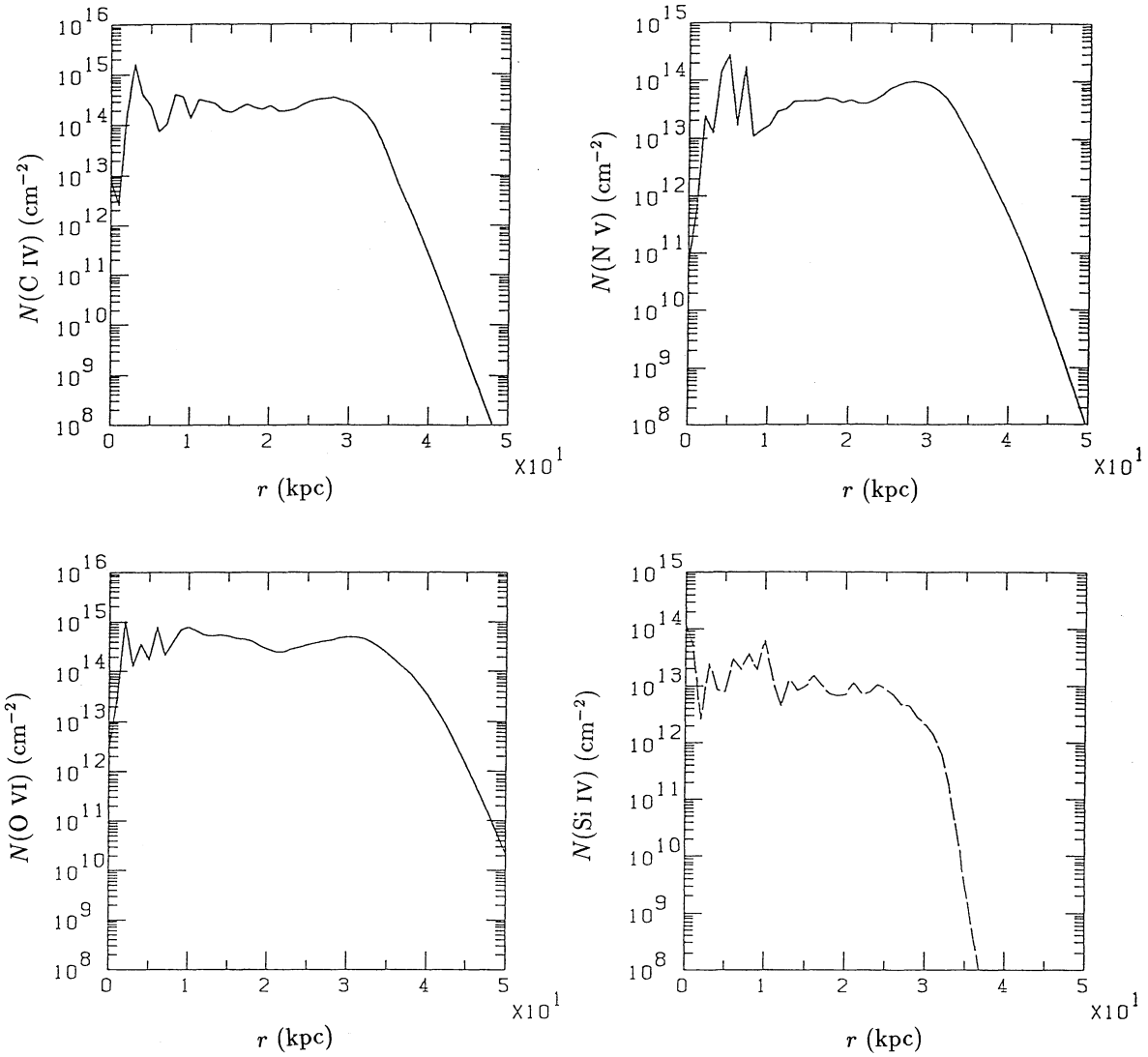

FIG. 12a

FIG. 12.—(*a*) Variations of the column densities [N(C IV), N(N V), N(O VI), and N(Si IV)] with r-coordinate which are integrated along r = constant for the *b-c* type halo. (*b*) Variations of the column densities with z-coordinate which are integrated along z = constant for the *b-c* type halo.

kiloparsecs to 100 kpc, which indicates that the gas temperature T_0 at the disk-halo interface should be quite high.

5.1. C IV *and* Si IV *Systems*

C IV and Si IV absorptions have only been observed in high-redshift systems ($Z > 1$) up to now, because for them the wavelengths of the doublets of C IV and Si IV shift into the optical range, which is possible to observe by using ground-based telescopes.

We construct a model for the C IV absorption system at the redshift $Z = 1.5$, because several high-resolution observations are available at around this redshift which can be compared with our calculations in detail. In such a high redshift ($Z > 1$), the heavy elements are underabundant compared with the solar abundance by a factor of 10 or so (Blades 1987). We assume an abundance to be 0.1 that of solar. Also, the flux of UV photons increases from the nearby value according to the $(Z + 1)^4$ law. The cooling rate due to heavy elements is10 times reduced in the calculation. The parameters at the disk-halo interface are adopted to be $T_0 = 6 \times 10^6$ K and $n_0 = 0.1$ cm^{-3}. The resultant mass and energy ejection rates are 230 $M_\odot$ yr^{-1} and 2.6×10^{43} ergs s^{-1}, respectively.

In Figure 13 we show the variations of the column densities with the r-coordinate. These column densities are integrated along r = constant throughout the halo. The column density of C IV is about 4×10^{15} cm^{-2} up to $r \sim 20$ kpc and decreases to 10^{13} cm^{-2} at $r \sim 60$ kpc. The column density of Si IV keeps about 5×10^{14} cm^{-2} up to $r \sim 10$ kpc and decreases rapidly to 10^{13} cm^{-2} at $r \sim 20$ kpc.

In Figure 14 we show the variations of the column densities with the z-coordinate. These column densities are integrated along z = constant throughout the halo. In contrast to Figure 13, the column densities are very low near the galactic disk, since the temperature is very high and the gas is fully ionized. The column densities increase with z and reach 10^{15} cm^{-2} for C IV and 10^{14} cm^{-2} for Si IV at $z \sim 30$ kpc. Then N(C IV) almost does not change until $z \sim 100$ kpc, while N(Si IV) keeps constant until $z \sim 70$ kpc and decreases to 10^{13} cm^{-2} at

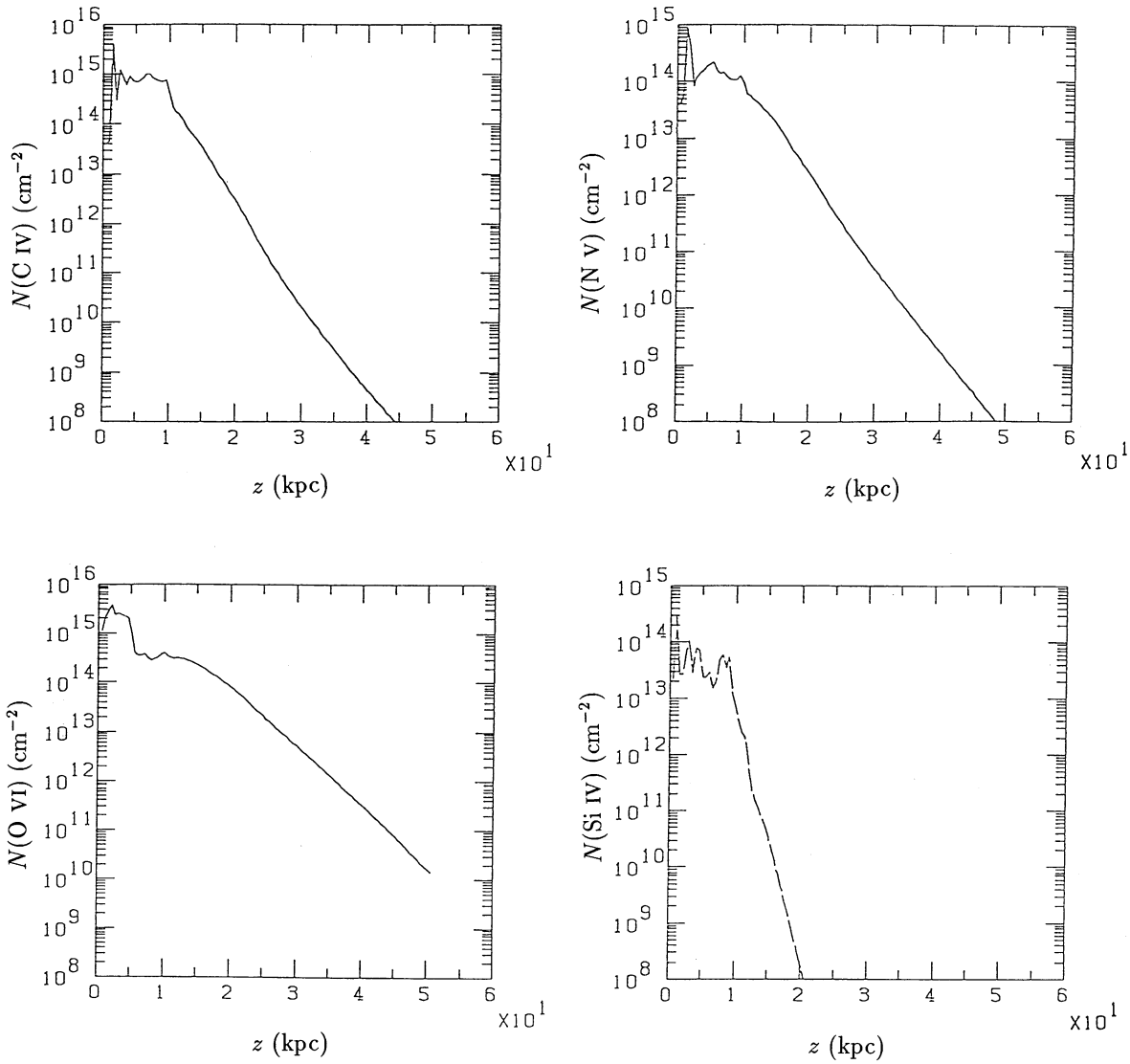

FIG. 12*b*

$z \sim 100$ kpc. This model is of a wind-type halo with high scale height of the gas. The variation of column density in Figure 14 reflects the temperature variation. At low z, the temperature is high and the gas is fully ionized, so that column densities are very small even if the gas density is high. The temperature decreases with increasing z, and the column densities increase. Due to the decrease of density, the column densities reach a maximum value at a certain height and decrease afterward.

We see from Figures 13 and 14 that the ratio N(Si IV)/N(C IV) is about 0.1 at the most abundant places in this model. The amount of C II is 3 times smaller than the amount of C IV. As mentioned in § 4.1, this is contrary to the halo of our Galaxy and consistent with the observations of QSO absorption-line systems. This can be understood by noting that the temperature is higher than in the model of our Galaxy and the ionization level is high compared with our Galaxy.

Recently, several high-resolution observations have been performed on C IV systems (York et al. 1984; Blades et al. 1985; Sargent, Steidel, & Boksenberg 1988b). It is shown that when the resolution is as high as 10 km s^{-1}, several components can be resolved in one object which gives information about the internal structure of the absorption systems. We show the velocity structure of the column density according to our result in Figure 15, which is the column density of C IV and Si IV integrated along $r = 20$ kpc. It is seen that when the resolution is as low as 30 km s^{-1}, we only see a broad absorption profile between 0 and $\sim$600 km s^{-1}. However, if the resolution is increased to 10 km s^{-1}, more than 10 components can be resolved. Each of them has column density greater than 10^{13} cm^{-2}. If we increase the resolution further, more components will be resolved.

5.2. Mg II *and* Ca II *Systems*

As Mg II and Ca II absorptions are observed in lower redshift systems, we calculate a model with redshift $Z = 0.3$ and metal abundance half that of solar. The parameters in the disk-halo interface are $T_0 = 3 \times 10^6$ K and $n_0 = 10^{-2}$ cm^{-3}, which correspond to a bound-type halo.

The resultant column densities are shown in Figure 16. In contrast to the wind-type halo, the detectable column densities are restricted to a small region ($r < 10$ kpc and $z < 10$–20 kpc) near the host galaxy and decrease rapidly with r and z, since

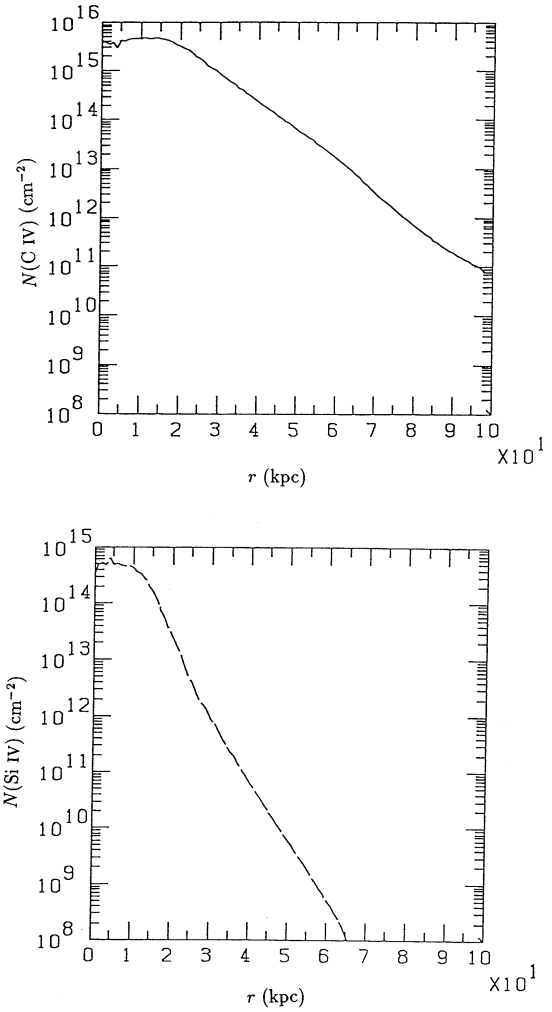

FIG. 13.—Variations of the column densities [N(C IV) and N(Si IV)] with r-coordinate which are integrated along r = constant.

the scale length is small. C IV and Si IV ions are detectable in the region $r < 20$ kpc and $z < 30$ kpc in this model. The z-variation of the column density is different from that in the wind-type halo because of low scale height.

The detectable column densities of Mg II and Ca II are restricted to a small region where the temperature is not too high and the density is not too low, not so different from the wind-type halos except that in the bound-type halo the detectable column densities are confined to a region with low scale height above the galactic plane, while in the wind-type halo, it is blown up to a region high above the galactic plane as described above. In the bound-type halos, the observable region is $r \leq 10$ kpc and $z \leq 10$ kpc, which seems to be consistent with the observations (Blades 1987). It is more difficult to produce detectable column density of Ca II with large scale height. The column density of Ca II is about 10 times smaller than that of Mg II, and the detectable region is smaller, especially in the r-direction, restricted to $r < 5$ kpc in our model. Since the column density and cross section of the absorption halos are small, it is not surprising that no Ca II absorption is observed in some galaxies (Blades 1987). It is reported that some Mg II absorption systems with redshifts greater than 0.5 are observed far from the host galaxies (~ 50 kpc) (Bergeron 1987). These correspond to the wind-type halo with a small detectable region high above the disk. In Figure 17 we show the resultant variation of Mg II column density with z-coordinate of the model in § 5.1. The variation is similar to that of C IV and Si IV, but it decreases faster beyond the height of maximum column density. It is seen that, in this case, the observable region is restricted to $z \sim 40$–60 kpc.

6. SUMMARY AND DISCUSSIONS

6.1. *Summary*

Formation of a galactic gaseous halo is simulated by using a two-dimensional hydrodynamic code based upon the chimney model of the interstellar medium. Radiative cooling, UV heating, and galactic gravity and rotation are taken into consideration. The abundance of each ion of C, N, O, Mg, Si, and Ca is calculated assuming ionization-recombination equilibria. We also simulate cloud condensation in the gaseous halo due to thermal instability and their motion in the galactic gravitational field.

The conclusion is that the resultant gaseous halo can be divided into three types according to the parameters at the disk-halo interface. If T_0 is greater than the critical temperature

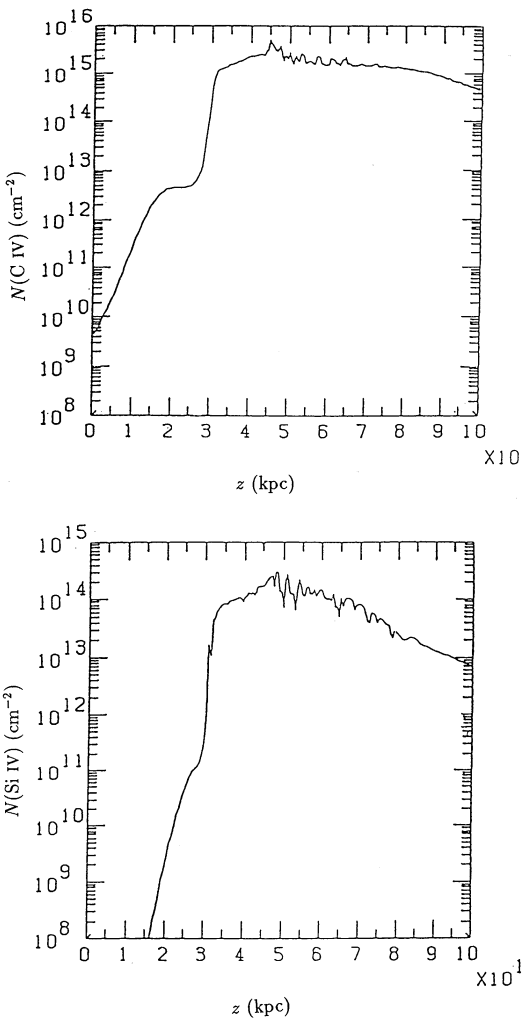

FIG. 14.—Variations of the column densities [N(C IV) and N(Si IV)] with z-coordinate which are integrated along z = constant.

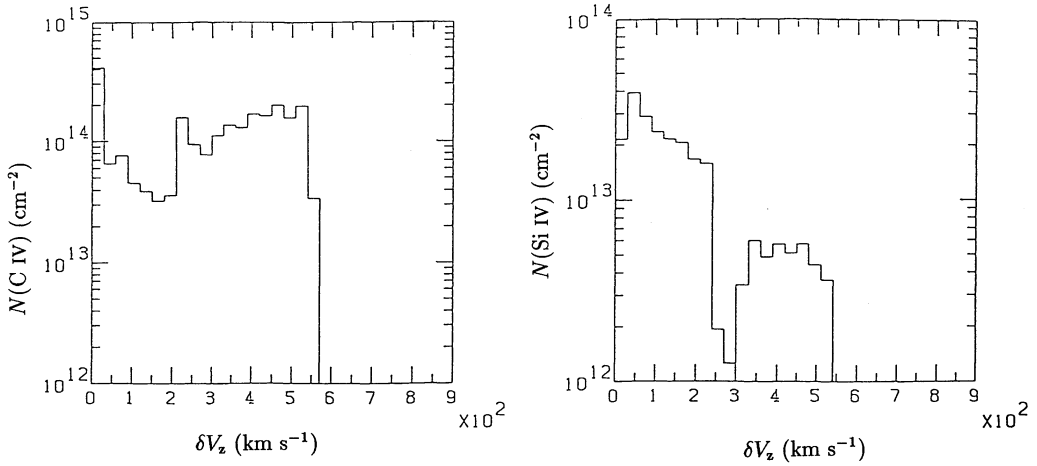

FIG. 15*a*

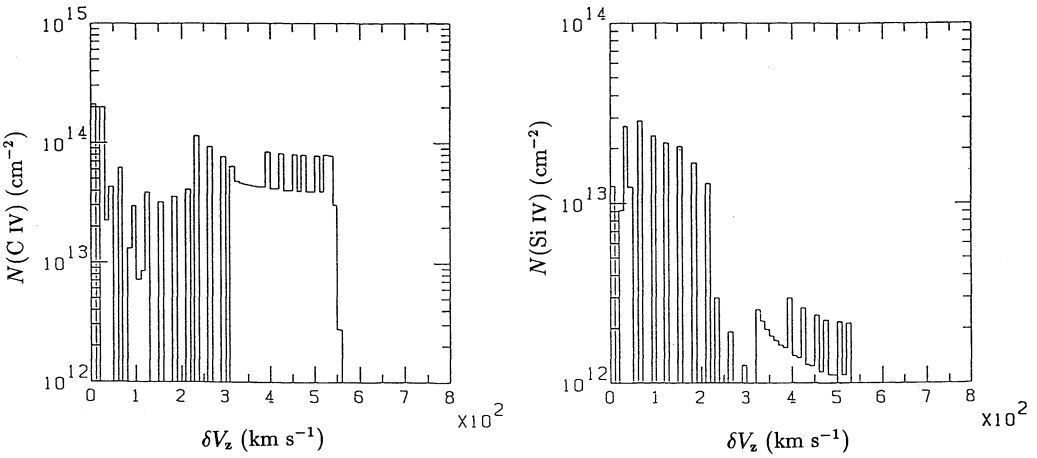

FIG. 15*b*

FIG. 15.—Profiles of C IV and Si IV absorption along $r = 20$ kpc with different velocity resolutions: (*a*) The result with resolution 30 km s^{-1}, in which we can only see a broad absorption profile. (*b*) The result with resolution 10 km s^{-1}, in which we can see over 10 components of C IV absorption and eight components of Si IV absorption in one object.

T_{cr} and radiative cooling is not efficient, all the gas ejected from the disk will escape from the galaxy to become a galactic wind. This is called the wind-type halo. If T_0 is smaller than T_{cr}, the gas is bound in the galaxy and returns to the outer galactic plane eventually. This is called the bound-type halo. If the gas density is high, so that radiative cooling becomes efficient, the gas is thermally unstable and condenses into cold clouds which are drawn out of the fluid and fall ballistically to the galactic disk. This is called a cooled-type halo. The cooled-type halos can further be divided into two classes according to their dynamical behavior. If T_0 is greater than T_{cr}, the global behavior of the gaseous halo is similar to that of the wind-type halo, and clouds are formed in a local region; this halo is called the *w-c* type. When T_0 is smaller than T_{cr}, the structure of the halo is similar to that of the bound-type halo, and a large amount of the gas condenses into clouds before moving far; this halo is called the *b-c* type.

We show in this work that galaxies like our own belong to the *b-c* type halo with 5×10^5 K $\leq T_0 \leq 10^6$ K and 10^{-3} cm^{-3} $\leq T_0 \leq 10^{-2}$ cm^{-3}. When integrated vertically from the Sun, the resultant column densities are N(C IV) $\sim 10^{14}$ cm^{-2}, N(N V) $\sim 10^{13}$ cm^{-2}, and N(Si IV) $\sim 10^{13}$ cm^{-2}, with scale height between 3 and 4 kpc, which conform to the observations well (Savage 1987). We also predict that the column density of O VI should be greater than $\sim 10^{14}$ cm^{-2} if absorption is observed in spectra of stars above 3–4 kpc. The column density of the low-ionized species C II is several times greater than that of the highly ionized species C IV.

We also find that the predicted distribution of H I clouds in (l, b) coordinates is roughly consistent with the whole-sky survey of high-velocity clouds except for the asymmetry between $b > 0$ and $b < 0$, namely:

1. Negative-velocity clouds are superior in the first and second quadrants in Galactic coordinates, while positive-velocity clouds are dominant in the third and fourth quadrants. This is the result of small z-velocity of the clouds, and the observed line-of-sight velocities are determined mainly by the differential rotation.

2. Most of the clouds are located at lower Galactic latitudes with $|b| < 40°$, which is the result of low scale height of the gas. We see from Figure 11 that about 50% of the clouds are located in the region $|l| < 60°$ and $b < 20°$. This is because we are observing the clouds across the Galactic center, so that

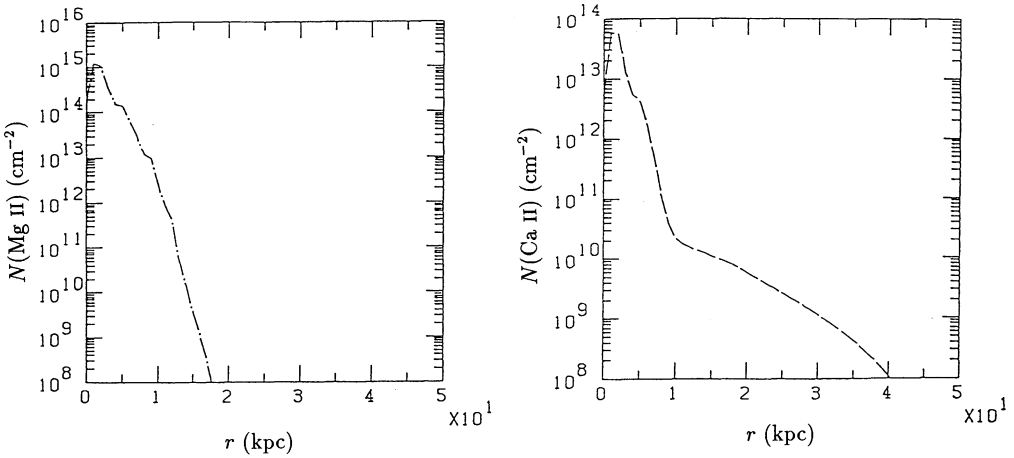

FIG. 16*a*

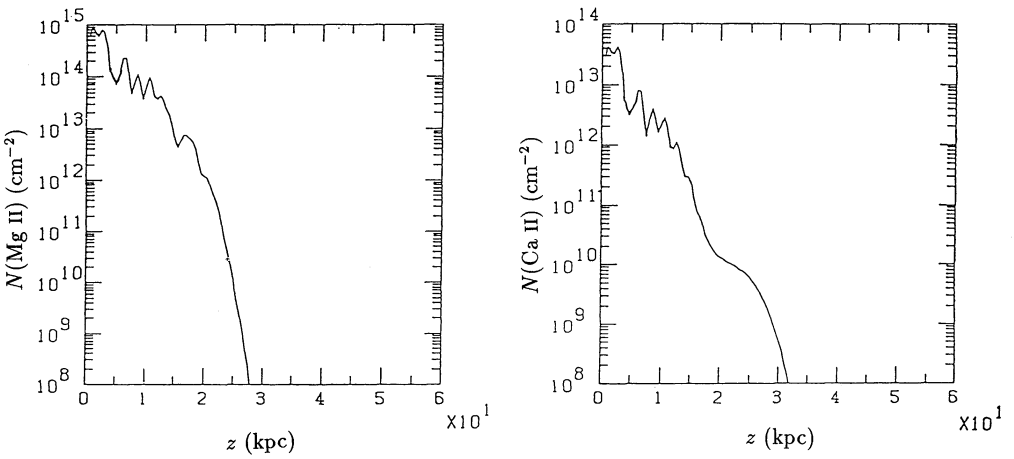

FIG. 16*b*

FIG. 16.—(*a*) Variations of the column densities [N(Mg II and N(Ca II)] with r-coordinate which are integrated along r = constant. (*b*) Variations of the column densities with z-coordinate which are integrated along z = constant.

even the clouds high above the Galactic plane have low latitudes due to the large distances from the observer. On the other hand, at the position of the anticenter, most of the clouds have higher latitude, since they are relatively nearby.

3. Most of the clouds with high line-of-sight velocities $|U| < 130$ km s^{-1} are located at lower Galactic latitudes with $|b| < 40°$, while the intermediate-velocity clouds with $|U| < 80$ km s^{-1} can be seen in any region.

We also simulated the giant gaseous halo around younger, distant galaxies observed as the absorption-line systems of heavy elements in the spectra of quasars. We find that in order to produce the observed C IV with sizes 50–100 kpc, the temperature at the disk-halo interface should be as high as $T_0 \geq 5 \times 10^6$ K, which leads to a wind-type halo in our calculation. In this case, the variation of the column densities of the ions with heights above the galactic plane is different from that of the bound-type halo; that is, the column density from a very small value at the base of the halo, to a detectable value at some height (30 kpc in our calculated model), reaches a maximum value at some height and decreases slowly. This is the result of gas-temperature distribution and ion density in the halo. The gas near the halo base is fully ionized and cannot be observed as absorption-line systems. The temperature decreases with the height above the plane, and column density increases because of the recombinations of the gas, and it gradually becomes detectable as absorption lines. Since the density decreases with the height, the column density reaches a maximum value and decreases afterward. Hence, the observed absorption-line systems with great distances from the host galaxies are actually undetectable if the line of sight to the quasars passes through the lower halo only. The scale length of the gas in the r-direction is not so large in this case (~ 30 kpc), since in a wind-type halo the gas moves in the z-direction faster than in the r-direction. We mentioned that the ratio of the column densities of C IV and Si IV is about 10 in most abundant regions for both ions, and the column density of C II is several times smaller than that of C IV, which is contrary to the model of the galaxies like our own. Furthermore, if we increase the velocity resolution, the absorber splits into subcomponents in the velocity range of several hundreds of kilometers per second, due to its internal velocity fields, and we hope by higher velocity resolution ($\lesssim 10$ km s^{-1}) observations to resolve the internal structure of the absorbers.

In contrast to the wind-type halo, in bound-type halos the column density decreases with height above the galactic plane,

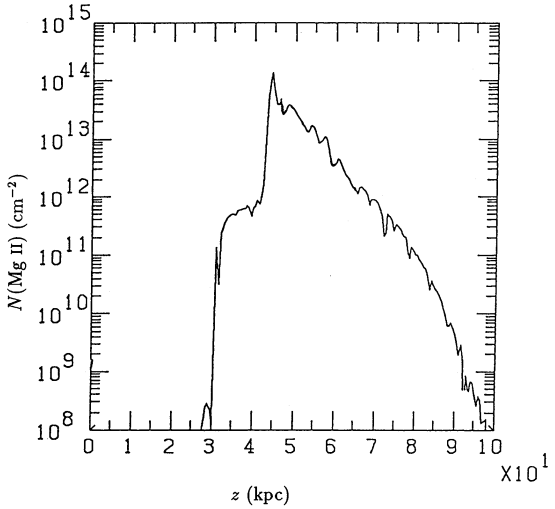

FIG. 17.—Variations of the Mg II column densities with z-coordinate which are integrated along z = constant for the wind-type halo.

since the gas temperature and scale height are lower compared with wind-type halos. Thus, the ionized ions are detectable only in a very small region not far from the host galaxies. The column densities of Mg II and Ca II are only detectable in a very restricted region both in wind-type and bound-type halos. Since the Ca II absorption systems are only observed with small sizes (20 kpc or so), we may think that they correspond to the bound-type halos.

6.2. *Discussion*

Compared with previous models, our calculations confirm the classification of gaseous halos by Habe & Ikeuchi (1980). We also find parameter ranges for the model of our Galaxy and the corresponding velocity distributions of the high-velocity clouds similar to the results of Bregman (1980). Moreover, we predict the percentage of the clouds in each region in Galactic coordinates. Recently, Houck & Bregman (1990) tried to explain the H I clouds at a lower halo region with smaller velocities by a low-temperature galactic fountain. They concluded that a fountain with $T_0 \sim 3 \times 10^5$ K gives the best explanation of this gas component. However, in order to offer an explanation of the clouds with high velocities, a higher temperature is necessary according to previous and present studies. The lower gas might arise from either the decelerated high-velocity clouds due to the drag force or a lower temperature gas component in the disk. Another deficiency of previous works is that they did not calculate the ionization structure of the gaseous halo, which is also very important in comparing the simulation with observations. By assuming an ionization equilibrium, we calculate the abundance of each ion of various elements and confirm that the observed column densities of C IV, N V, O VI, and Si IV in the Galactic halo can be explained by our model. In the same way, we also investigate what we can say about the absorption-line systems of QSOs by the present model.

To sum up, the Galactic gaseous halo and absorption-line systems of heavy elements in the spectra of quasars can be explained with the same mechanism—hot gas ejection from the galactic disk to the halo—but with different parameters at the disk-halo interface. There are many interesting subjects to investigate in the future, such as the halo response to the time variable disk activities. As mentioned earlier and in Papers II and III, it is possible that the disk-halo system undergoes a periodic evolution in starburst galaxies with a time scale of order 10^9 yr. Since the effect of the magnetic field is comparable to that of the gas pressure in the Galaxy, it is necessary to examine the connected disk-halo system taking into account the magnetic field.

A tentative observed column density distribution of the Mg II system has been obtained by Petitjean & Bergeron (1990). They get a best fit by a power-law distribution $dn/dN(\text{Mg II}) \propto N(\text{Mg II})^{-\beta}$ with $\beta = 1.0 \pm 0.1$. We select 13 points with column densities between 10^{12} and 10^{15} cm^{-2} and plot the Mg II column density distribution in Figure 18 for the present model. The differential number dn is assumed to be proportional to the corresponding differential cross section of the absorber with column density N(Mg II), i.e., $dn \propto 2\pi z\, dz$ where z is the height above the galactic plane. The solid line is the best fit to a power-law distribution with $\beta \sim 1.13$, which is not too different from the observed result. The internal structure of our calculated halo is consistent with the observed absorption-line systems.

We believe that the observed variation of the number densities of absorption-line systems with redshift is the result of the evolution of star formation activity of host galaxies. We have already shown in the present work that the evolution of disk activity does give rise to the evolution of absorption-line systems from a giant absorbing halo (greater than 50 kpc) to a halo with size comparable to the optical range. Because of the increasing amount of data obtained by the *Hubble Space Telescope*, the information about the absorption-line systems will

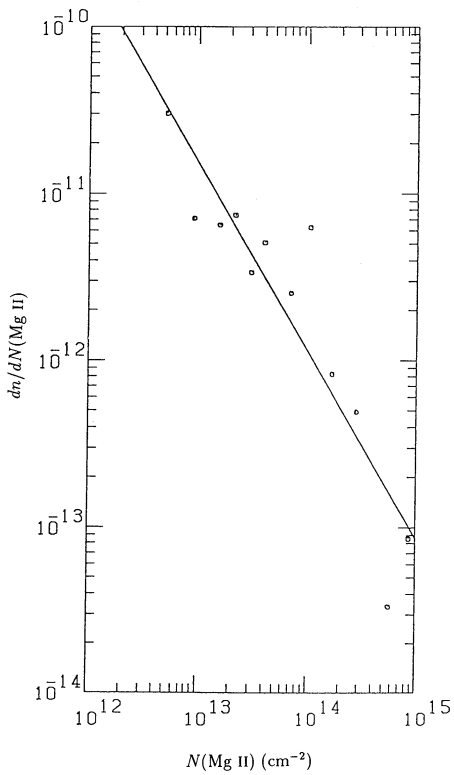

FIG. 18.—Column density distribution of Mg II systems. The solid line is the best fit to a power-law spectrum with index $\beta \sim 1.13$.

cover all of the redshift range. This will help us to search for the whole history of galactic evolution.

The authors gratefully acknowledge colleagues of the theoretical astrophysics division of the National Astronomical Observatory for many valuable discussions. Special thanks are due to S. Yoshioka for kindly offering the computational code. One of the authors (F. L.) acknowledges the scholarships from the Ministry of Education, Science, and Culture of Japan for graduate studies of foreign students. The numerical calculations were performed by Facom-M780 at the National Astronomical Observatory and by Facom-VP200 at the Nobeyama Radio Observatory.

REFERENCES

Bajaja, E., Cappa de Nicolau, C. E., Cersosimo, J. C., Loiseau, N., Martin, M. C., Morras, R., Olano, C. A., & Poppel, W. G. L. 1985, ApJS, 58, 143
Bergeron, J. 1987, in QSO Absorption Lines: Probing the Universe, ed. J. C. Blades, D. A. Turnshek, & C. A. Norman (Cambridge: Cambridge Univ. Press), 127
Black, J. H. 1981, MNRAS, 197, 553
Blades, J. C. 1987, in QSO Absorption Lines: Probing the Universe, ed. J. C. Blades, D. A. Turnshek, & C. A. Norman (Cambridge: Cambridge Univ. Press), 147
Blades, J. C., Hunstead, R. W., Murdoch, H. S., & Pettini, M. 1985, ApJ, 288, 580
Bloemen, H., ed. 1990, IAU Symp. 144, The Interstellar Disk-Halo Connection in Galaxies (Dordrecht: Reidel)
Bregman, J. N. 1980, ApJ, 236, 577
———. 1981, ApJ, 250, 7
Brinks, E., & Bajaja, E. 1986, A&A, 169, 14
Butler, S. E., Heil, T. G., & Dalgarno, A. 1980, ApJ, 241, 442
Cash, W., Charles, P., Bowyers, S., Walter, F., Garmire, G., & Riegler, G. 1980, ApJ, 238, L71
Dalgarno, A., & McCray, R. A. 1972, ARA&A, 10, 375
Danly, L. 1989, ApJ, 342, 785
Danly, L., Blades, J. C., & Norman, C. A. 1987, in QSO Absorption Lines: Probing the Universe, A Collection of Poster Papers, ed. J. C. Blades, D. A. Turnshek, & C. A. Norman (Cambridge: Cambridge Univ. Press), 88
Davis, R. D. 1972, Nature, 237, 88
———. 1973, MNRAS, 160, 381
de Boer, K. S. 1989, in IAU Colloq. 120, Structure and Dynamics of the Interstellar Medium, ed. G. Tenorio-Tagle, M. Moles, & J. Melnick, (Berlin: Springer), 432
———. 1990, in IAU Symp. 144, The Interstellar Disk-Halo Connection in Galaxies, ed. J. B. G. M. Bloemen (Dordrecht: Reidel), in press
Deul, E. R., & den Hartog, R. G. 1990, A&A, 229, 362
Deul, E. R., & van der Hulst, J. M. 1987, A&AS, 67, 509
Field, G. B. 1965, ApJ, 142, 531
Habe, A., & Ikeuchi, S. 1980, Prog. Theor. Phys., 64, 1995
Heiles, C. 1979, ApJ, 299, 533
———. 1984, ApJS, 55, 585
———. 1987, ApJ, 315, 555
———. 1990, ApJ, 354, 483
Houck, J. C., & Bregman, J. N. 1990, ApJ, 352, 506
Hulsbosch, A. N. M. 1975, A&A, 40, 1
Hulsboch, A. N. M., & Wakker, B. P. 1988, A&AS, 75, 191
Ikeuchi, S. 1987, in Starbursts and Galaxy Evolution, ed. T. X. Thuan, T. Montmerle, & J. Tran Thanh Van (Paris: Editions Frontières), 27
———. 1988, Fund. Cosmic Phys., 12, 255
Innanen, K. A. 1973, Ap&SS, 22, 393
Itoh, M., & Ikeuchi, S. 1988, PASJ, 40, 403
Kamphuis, J., & Brinks, E. 1991, in preparation
Kamphuis, J., Sancisi, R., & van der Hulst, T. 1991a, A&A, 244, L29
Kamphuis, J., van der Hulst, T., & Sancisi, R. 1991b, in preparation
Koyama, K., Makishima, K., Tanaka, Y., & Tsunemi, H. 1986, PASJ, 38, 121
Li, F., & Ikeuchi, S. 1989, PASJ, 41, 221 (Paper I)
———. 1990a, ApJS, 73, 401 (Paper II)
———. 1990b PASJ, 42, 387 (Paper III)
McKee, C. F., & Ostriker, J. P. 1977, ApJ, 215, 213
Miyamoto, F., & Nagai, S. 1975, PASJ, 27, 533
Norman, C. A., & Ikeuchi, S. 1989, ApJ, 345, 372
Norman, M. L., & Winkler, K.-H. A. 1986, in Astrophysical Radiation Hydrodynamics, ed. K.-H. A. Winkler & M. L. Norman (Dordrecht: Reidel), 187
Nussbaumer, H., & Storey, P. J. 1983, A&A, 126, 75
Oort, J. H. 1966, Bull. Astr. Inst. Netherlands, 18, 421
———. 1967, in IAU Symp. 31, Radio Astronomy and the Galactic System, ed. H. van Woerden (Dordrecht: Reidel), 279
———. 1969, Nature, 224, 1158
———. 1970, A&A, 7, 381
Petitjean, P., & Bergeron, J. 1990, A&A, 231, 309
Raymond, J. C., Cox, D. P., & Smith, B. W. 1976, ApJ, 204, 290
Reilman, R. F., & Manson, S. T. 1979, ApJS, 40, 815
Robertson, J. G., Schwarz, U. J., van Woerden, H., Murray, J. D., Morton, D. C., & Hulsbosch, A. N. M. 1991, MNRAS, 248, 508
Sargent, W. L. W., Steidel, C. C., & Boksenberg, A. 1988, ApJ, 334, 22
Savage, B. D. 1987, in QSO Absorption Lines: Probing the Universe, ed. J. C. Blades, D. A. Turnshek, & C. A. Norman (Cambridge: Cambridge Univ. Press), 195
Savage, B. D., & de Boer, K. S. 1979, ApJ, 230, L77
Savage, B. D., & Massa, D. 1987, ApJ, 314, 380
Shapiro, P. R., & Field, G. B. 1976, ApJ, 207, 406
Shull, J. M., & van Steenberg, M. 1982, ApJS, 48, 95
Songaila, A. 1981, ApJ, 243, L19
Songaila, A., Cowie, L. L., & Weaver, H. F. 1988, ApJ, 329, 580
Songaila, A., York, D. G., Cowie, L. L., & Blades, J. C. 1985, ApJ, 293, L15
Spitzer, L. 1956, ApJ, 124, 20
van der Hulst, J. M., & Sancisi, R. 1988, AJ, 95, 1354
van Leer, B. 1977, J. Comput. Phys., 23, 276
van Woerden, H., Schwarz, U. J., & Hulsbosch, A. N. M. 1985, in IAU Symp. 106, The Milky Way Galaxy, ed. H. van Woerden, R. J. Allen, & W. B. Burton (Dordrecht: Reidel), 387
van Woerden, H., Schwarz, U. J., & Wakker, B. P. 1989, in IAU Colloq. 120, Structure and Dynamics of the Interstellar Medium, ed. G. Tenorio-Tagle, M. Moles, & J. Melnick (Berlin: Springer), 389
Verschuur, G. L. 1973, A&A, 22, 139
Wakker, B. P. 1991, A&A, in press
Wakker, B. P., & van Woerden, H. 1991, A&A, in press
Warwick, R. S., Turner, M. J. L., Watson, M. G., & Willingale, R. 1985, Nature, 317, 218
West, K. A., Pettini, M., Penston, M. V., Blades, J. C. & Morton, D. C. 1985, MNRAS, 215, 481
Wolfe, A. M. 1983, ApJ, 268, L1
York, D. G., Green, R. F., Bechtold, J., & Chaffee, F. H. 1984, ApJ, 280, L1
Yoshioka, S., & Ikeuchi, S. 1990, ApJ, 360, 352